AN $H_2{}^{18}O$ WATER TARGET FOR THE PRODUCTION OF

^{18}F - FLUORIDE IN THE TR-13 CYCLOTRON

By

Roberto A. Pavan

B. A. Sc. (Engineering Physics) University of British Columbia

A THESIS SUBMITTED IN PARTIAL FULFILLMENT OF

THE REQUIREMENTS FOR THE DEGREE OF

MASTER OF APPLIED SCIENCE

in

THE FACULTY OF GRADUATE STUDIES

DEPARTMENT OF ENGINEERING PHYSICS

We accept this thesis as conforming

to the required standard

THE UNIVERSITY OF BRITISH COLUMBIA

December 1997

© Roberto A. Pavan, 1997

In presenting this thesis in partial fulfilment of the requirements for an advanced degree at the University of British Columbia, I agree that the Library shall make it freely available for reference and study. I further agree that permission for extensive copying of this thesis for scholarly purposes may be granted by the head of my department or by his or her representatives. It is understood that copying or publication of this thesis for financial gain shall not be allowed without my written permission.

Department of Engineering Physics

The University of British Columbia

6224 Agricultural Road

Vancouver, Canada

V6T 1Z1

Date: _Dec. 22/97_

Abstract

This thesis presents the design, operation, performance and heat transfer modeling of a ^{18}F production target for the EBCO/TRIUMF TR-13 cyclotron. This target employs the ^{18}O(p,n)^{18}F reaction in ^{18}O-enriched water.

Positron emission tomography (PET) depends upon the availability of short-lived positron-emitting radionuclides, such as, ^{11}C, ^{13}N, ^{15}O, for radiopharmaceutical syntheses. Among the most important of these radionuclides is ^{18}F ($t_{1/2}$=109.6 min). It is almost exclusively produced in small medical cyclotrons by proton bombardment of isotopically enriched ^{18}O-water in small volume targets. Production targets are required that can produce large quantities reliably, efficiently and economically. A key design component in such targets is the dissipation of heat generated as the proton beam is stopped within the target material.

In order to better understand the heat transfer mechanisms involved and their relation to production target design, an ^{18}F production target was constructed and a heat transfer model based on measurements was developed. The results derived from the model were in good agreement with the data from the irradiation experiments, in particular in the higher current regions that are required for high yield ^{18}F production. It is believed that the target discussed here can be successfully used in the routine production of ^{18}F in sufficient quantities and of adequate quality for *in vivo* applications.

Table of Contents

List of Tables

List of Figures

Acknowledgement

It's nice to be done, finally. I would like to thank everyone that helped, but there are really too many to list, and besides, you all know who you are—I hope. So thanks, everyone. I couldn't have done it without any of you.

...and I'm sorry it took so long.

To Mama and Papà

Chapter 1

Introduction

During the last decade, positron emission tomography (PET) has become the method of choice for many diagnostic applications in nuclear medicine. It is the most powerful tool for studying physiological, pharmacological and biochemical phenomena in oncology, neurology and other disciplines because it is the only non-invasive method that permits quantitative dynamical measurements of radioactivity *in vivo*. PET imaging is based on the detection of two photons originating from the annihilation of a positron and an electron within a narrow time interval (coincidence measurement). The patient receives a suitable quantity of a tracer substance labelled with a carrier-free positron-emitting nuclide such as ^{11}C, ^{13}N, ^{15}O or ^{18}F. These radionuclides can replace the corresponding stable isotope in a biologically active compound without altering its physiological properties. ^{18}F can be used as a substitute for a hydrogen atom or a hydroxyl group.

Many clinical PET studies involve measurements in the order of one to several hours and hence require the incorporation of a radiotracer with a half-life comparable to the observation time. ^{18}F, currently the most important radionuclide for PET, has a convenient half-life of 109.6 *min*, decays exclusively via positron emission ($E_{\beta,max} = 0.64$ *MeV*) and emits no additional γ-lines. It can be produced in high yield by proton bombardment of isotopically enriched ^{18}O. The nuclear reaction ^{18}O(p,n)^{18}F has a comparatively low threshold energy of $\approx$. 2.5 *MeV* which makes this production

1

process feasible for small proton accelerators. Depending on the chemical form of ^{18}F required for the subsequent radiopharmaceutical synthesis, ^{18}F has to be extracted from a gas target as molecular fluorine [^{18}F]F$_2$ or from a liquid target as fluoride [^{18}F]F$^-$. ^{18}F–fluoride is used worldwide for the preparation of the versatile imaging agent 2-fluoro-2-deoxyglucose (FDG).

The production of [^{18}F]fluoride is usually performed in a small volume target filled with isotopically enriched ^{18}O–water (> 95% ^{18}O). A common problem associated with this method is the formation of steam bubbles in the irradiated water during bombardment, especially at high beam currents. The gas bubbles have lower density than the liquid, *i. e.* fewer target nuclei are hit by the incident particles, which lowers the production rate of ^{18}F. In order to avoid this effect, boiling has to be minimized by efficient cooling of the target body. To provide optimal cooling, the material with which the target is constructed needs to have high thermal conductivity, and therefore many targets manufactured from silver have been described in the literature. However, the material of the target chamber has to be carefully chosen since many metals are known to form stable, unreactive complexes or insoluble compounds with fluorine which renders the product useless. Earlier investigations have shown that silver and titanium have the most suitable properties from the chemical point of view. Silver does not adsorb the fluoride irreversibly, but sometimes contamination of the target water with colloidal silver particles occurs which can cause problems in the radiochemical synthesis. Titanium targets are rapidly passivated and become inert with time. On the other hand, titanium is a poor heat conductor which makes cooling of the target difficult.

Few papers have been published on the heat transport mechanisms in ^{18}F production targets. [Votaw(1989)] and [Steyn(1990)] analyzed the beam-induced heating of helium-cooled target foils. [Bubb(1981)] analyzed the heat transfer of helium-cooled targets in high current electron beams. [Wojciechowski(1987)] provided some

discussion of heat transfer mechanisms in $[^{18}F]F_2$ gas targets. [Steinbach(1990)] provided some qualitative analysis on the magnitude of heat transfer mechanisms in an open water target, but stopped short at determining that conduction and free convection alone were not sufficient to cool the target, and that a mechanism involving water boiling could provide the necessary cooling power.

The principal goal of the study presented in this thesis was the development of a mathematical model for the simulation of the heat transfer in a small volume water target. This numerical model was designed to provide information on the heat transport mechanisms involved and their respective significance for the heat transfer out of the target. The results predicted by the computer simulation were analyzed and eventually compared to the experimental findings from test irradiations of a specifically designed titanium target body with 13 *MeV* protons at various beam currents.

Chapter 2

Theory

This chapter outlines some of the physics necessary for understanding some of the decisions involved in the design and operation of radionuclide production targets.

2.1 Nuclear and Target Physics

2.1.1 Interactions of Radiation with Matter

The theoretical relationship between the range of an energetic particle in matter and the energy of the projectile particle can be obtained from a quantum mechanical calculation of the collision process (Bethe-Bloch formula). The calculation provides the *stopping power*, or the magnitude of the energy loss per unit length [Krane, p.194], given by Equation 2.1:

$$\frac{dE}{dx} = \left(\frac{e^2}{4\pi\varepsilon_0}\right)^2 \frac{4\pi z^2 N_0 Z \rho}{mc^2\beta^2 A} \left[\ln\left(\frac{2mc^2\beta^2}{I}\right) - \ln\left(1-\beta^2\right) - \beta^2\right] \qquad (2.1)$$

where

$v = \beta c$ is the velocity of the projectile particle,

ze is the electric charge of the particle,

Z is the atomic weight of the stopping material,

A is the atomic number of the stopping material,

ρ is the density of the stopping material,

N_0 is Avogadro's number,

m is the electron mass,

I is the mean ionization potential.

The stopping material is often referred to as the target. Equation 2.1 can be integrated to determine the amount of energy loss in a given target thickness.

The mean range of the incident particles in the target can then be calculated by integrating Equation 2.1 over the energies of the projectile particle, as given by Equation 2.2 [Krane, p. 195]:

$$R = \int_T^0 \left(-\frac{dE}{dx} \right)^{-1} dE ,$$

(2.2)

where T is the kinetic energy of the projectile particle.

If all of the incident beam is stopped in the target material, it is said to be a *thick target*. If only a portion of the beam is stopped in the target material, the target is said to be *thin*.

2.1.2 Nuclear Reactions

Neutron-deficient radionuclides such as ^{18}F are produced through nuclear reactions achieved by bombarding stable nuclides with beams of charged particles which are produced in accelerators such as cyclotrons or linacs. The nuclei of the target capture the particle, triggering a reaction which leads to the production of the radioactive species. Figure 2.1 shows some of the more common nuclear reactions possible from a given nuclide.

Since this paper is concerned with a cyclotron production target, this bias will be reflected in subsequent sections. ^{18}F is most commonly produced in cyclotron irradiated production targets [Guillaume(1991)].

	α,4n ^{3}He,3n	α,3n ^{3}He,2n	α,2n ^{3}He,n	α,n	
p,3n	p,2n d,3n	p,n d,2n	p,γ ^{3}He,pn d,n	α,pn ^{3}He,p	
		p,pn d,t n,2n γ,np	**Target Nuclide**	α,2pn d,p n,γ	
p,αn	p,α	d,α γ,np	n,d γ,p	n,p	
		n,α	n,pd		

Figure 2.1: Displacement of radionuclides produced by nuclear reactions with light acceler-ated particles [Helus, p. 60]. Reactions are indicated by the incident particle separated by a comma from the particle(s) displaced from the original nucleus. In the figure above particle species are indicated by letter: p—proton; n—neutron; γ—γ-particle or photon; d—deuteron; α—α-particle or helium nucleus. For example, in the ^{18}O(p,n)^{18}F reaction, a proton is intro-duced to the ^{18}O nucleus and a neutron is displaced, transmuting the original nucleus from ^{18}O into ^{18}F .

Q-Value, Threshold Energy and Coulomb Barrier

The minimum energy required for a nuclear reaction to occur is determined by the conservation of mass-energy. The energy equivalent of the balance of masses before and after the reaction is called the "Q-value" and is defined as [Helus, p. 43]

$$Q = [(\text{Sum of atomic masses of reactants}) - (\text{Sum of atomic masses of products})]\cdot c^2$$

If Q is negative, energy must be introduced to the system for the reaction to take place. In the case of nuclear reactions caused by cyclotron beams, this energy is provided by the incident beam of particles.

In addition, a certain amount of kinetic energy must be provided due to the momentum transfer of the incident particle to the target nucleus. If the mass of the incident particle is given by m and the mass of the target nucleus is given by M, the minimum kinetic energy or *threshold energy* required for the reaction to occur, T_{min}, is given by

$$T_{min} = -Q\frac{m+M}{M} \,. \qquad (2.3)$$

The Q-value of the ^{18}O(p,n)^{18}F reaction is -2.4 *MeV* as calculated by this method [Keller, p. 58].

Another physical phenomenon that also adds to the actual threshold energy of a nuclear reaction is the Coulomb barrier which rises significantly when the positively charged particle approaches the nucleus:

$$E_C = \frac{Z_m Z_M e^2}{4\pi\varepsilon_0 r_{min}} \,, \qquad (2.4)$$

where Z_m, Z_M are the atomic numbers of the incident particle and the target nucleus, r_{min} is the distance between particle and nucleus.

Reaction Cross-Sections and Excitation Function

The probability of a nuclear reaction occurring is expressed in terms of an effective area or cross-section σ for the target nucleus as seen by the projectile particles. This quantity is not identical with, but often larger than the physical cross-sectional area. It is expressed in units of barns.

$$1 \text{ barn} = 10^3 \text{ millibarns } (mb) = 10^{-24} cm^2$$

Every nucleus exhibits a specific cross-section for each of the possible nuclear reactions and these cross-sections vary depending on the kinetic energy of the incident particle relative to the target nucleus. When the reaction cross-section is plotted as a function of energy, the result is referred to as the *excitation function* of the reaction.
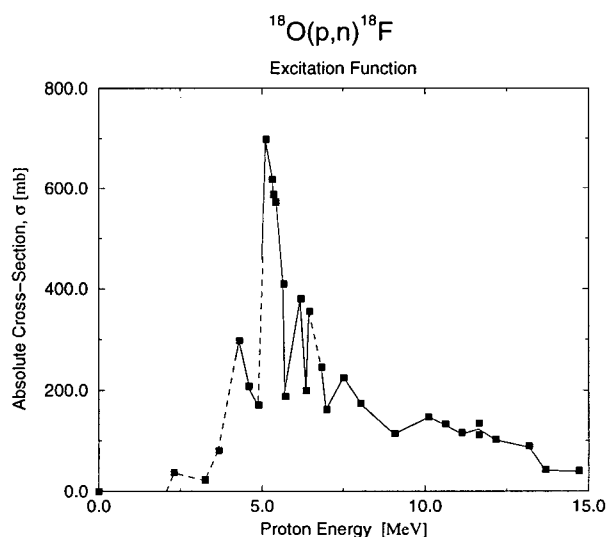
Figure 2.2: The cross-section of the ^{18}O(p,n)^{18}F reaction vs. proton energy [Ruth(1979)]. The dashed lines indicate points that were joined together to interpolate the given data set, but were not joined by the authors of the original paper.

2.1.3 Production of Radionuclides

Production Rate

If a particle beam hits a thin target, i. e. a target that degrades the incident energy by a very small amount, the number of produced nuclei N_P per volume unit can be determined as

$$N_P = N_0 \sigma I \Delta x \tag{2.5}$$

where I is the beam current, σ is the reaction cross section, Δx is thickness of the thin target and N_0 is the number of target nuclei per volume unit which is calculated as

$$N_0 = \frac{\rho}{M} N_L . \tag{2.6}$$

ρ is the density of the target material, M is the molecular weight and N_L is Avogadro's number. To relate to the numbers per gram, simply divide Equation 2.5 by ρ:

$$n = n_0 \sigma I \Delta x \tag{2.7}$$

Assuming the product nuclei decay to a stable nuclide with a decay constant λ, the build-up equation can be obtained by integration over the irradiation time t_{irr}:

$$n(t_{irr}) = n_0 \sigma I \Delta x \frac{1}{\lambda} [1 - exp(-\lambda t_{irr})] \tag{2.8}$$

The number of radioactive nuclei at a certain time t_m after the end of bombardment (EOB) is given by

$$n(t_{irr}, t_m) = n_0 \sigma I \Delta x \frac{1}{\lambda} [1 - exp(-\lambda t_{irr})] \cdot exp(-\lambda t_m) . \tag{2.9}$$

Radioactive Decay

The radioactivity of a given number of nuclei can easily be calculated from the first derivative of equation 2.9:

$$-\frac{dn}{dt_m} = n_0 \sigma I \Delta x [1 - exp(-\lambda t_{irr})] \cdot exp(-\lambda t_m) . \tag{2.10}$$

The decay of radioactive materials is statistical in nature and follows an exponential law. It is impossible to predict when any given atom will spontaneously disintegrate. A convenient unit of measure of radioactivity is the *becquerel* (*Bq*), which is equal to one decay per second. The former unit called the *curie* (*Ci*) indicted the radioactivity of one gram of radium:

$$1 \ Ci = 3.7 \times 10^{10} \text{ decays/s} = 3.7 \times 10^{10} \ Bq \ .$$

The curie is still commonly used and will be the unit of choice for the remainder of this report.

Thick Target Activity

In a thick target the incident energy is degraded to the threshold energy E_{thr}, and the produced activity at EOB ($t_m = 0$) can be obtained by integration of Equation 2.10 over the energy range. With $\Delta x = \frac{\Delta E}{E/dx}$ the formula can be written as

$$A_{EOB} = - \int_{E_{thr}}^{E_{max}} \frac{dn}{dt} = In_0[1 - \exp(-\lambda t_{irr})] \int_{E_{thr}}^{E_{max}} \frac{\sigma(E)}{dE/dx} dE \qquad (2.11)$$

When irradiating the target for a period of time much longer than the half life, the exponential in Equation 2.11 approaches zero, and the activity becomes constant. In this case the target is said to be at its *saturation activity*, the maximum possible:

$$A_{sat} = In_0 \int_{E_{thr}}^{E_{max}} \frac{\sigma(E)}{dE/dx} dE \qquad (2.12)$$

In order to establish a convenient measure for the production of radioactivity, it is necessary to normalize the radioactivity:

Saturation Yield The saturation yield is given in units of activity per unit current at the energy of the incident particles on the target, I is the irradiating beam current, and t_{irr} is the target irradiation time [Solin(1988)]:

$$Y_{sat} = \frac{A_{EOB}}{\left[1 - \exp\left(\frac{-\ln 2 \cdot t_{irr}}{T_{1/2}}\right)\right] \cdot I} \qquad (2.13)$$

Figure 2.3 shows the saturated yield of the $^{18}O(p,n)^{18}F$ reaction in mCi per micro-amp as it varies with proton energy.
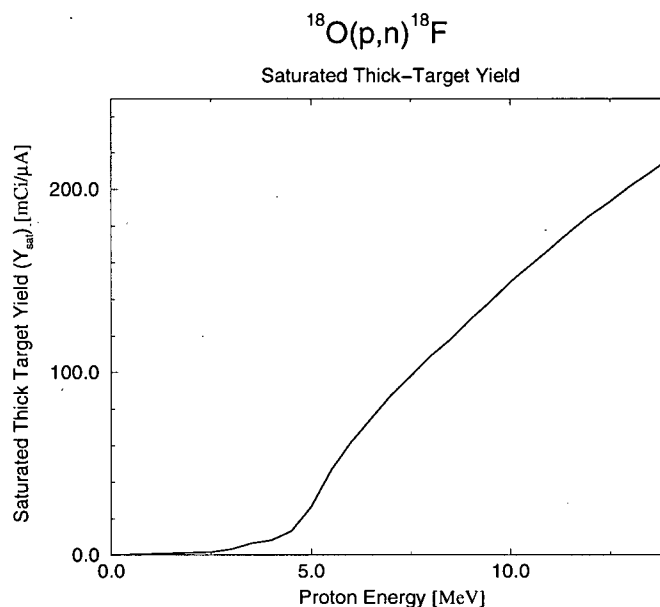
Figure 2.3: Saturated yield curve for the production of ^{18}F from the $^{18}O(p,n)^{18}F$ reaction as a function of energy [Ruth(1979)].

Production Yield The radioactivity at EOB is divided by the integrated beam current and the irradiation time:

$$Y_{prod} = \frac{A_{EOB}}{I \cdot t_{irr}} \tag{2.14}$$

In [Guillaume(1991)] a convenient table of theoretical production rates for the $^{18}O(p,n)^{18}F$ reaction on 100 %-enriched ^{18}Owater targets was prepared, basing the data on the work of [Ruth(1979)]. This is reprinted in Table 2.1.3.

Since the cost of using an accelerator is often in direct proportion to the irradiation time, if is most economical to produce activity by remaining within the linear regime ($t \ll t_{1/2}$). Thus, in order to economically produce large amounts of radionuclides, the

Ep (MeV)	Range in Water (mg/cm²)	Production Rate (mCi/µAh)
4	23.3	2.2
5	34.5	6.4
6	47.6	16.2
7	62.7	23.2
8	79.6	28.9
9	98.3	33.8
10	119	39.1
11	140	43.8
12	165	48.4
13	190	52.2
14	216	54.5
15	246	56.4
16	277	58.0
17	312	59.5
18	345	60.5
19	378	61.4
20	415	62.1
21	445	62.5
22	480	62.7

Table 2.1: Proton range in water and production rate of ^{18}F from a 100 % ^{18}O-enriched water target as a function of proton energy [Guillaume(1991)].

production rate must be increased. This can be achieved by any combination of factors, such as choosing the reaction with the largest possible cross-section, increasing the current of bombarding particles, or increasing the size of the target.

Target Efficiency

A measure of the efficiency of a target, is how much activity it produces under a given beam current and energy, relative to the theoretical amount given by Equation 2.13. Since activity measurements can occur at any time after the irradiation of the production target, activity measurements can vary greatly. For this reason, it

is customary to quote the activity produced by a production target at the time bombardment ends. This is referred to as the *end of bombardment* (EOB) activity. If the end of bombardment time is noted, t_{EOB}, as well as the time of the activity measurement, t_2, and only one species is present, the EOB activity is easily calculated from the definition of the exponential law, and is given in Equation 2.15.

$$A_{EOB} = \frac{A(t_2)}{e^{-\lambda(t_2 - t_{EOB})}}$$
(2.15)

The ratio of the EOB activity to the theoretical value provides a useful measure target performance.

2.2 Heat Transfer

During proton irradiation, the production target receives an input of energy equal to the energy of the proton beam deposited in the target times the beam current. This amounts to 120–480 *W* in the target described in Chapter 3. To avoid catastrophic failures such as foil ruptures or the melting of target components, this energy must be removed. In this target, cooling is provided by the forced convection of helium on the target window, and water to the back of the target cell and through the target body. In order to provide a better understanding of the heat transfer model, a short explanation of steady-state heat transfer concepts will now be provided[1]. There are three major modes of heat transport: conduction, convection and radiation.

2.2.1 Conduction

When a temperature gradient exists in a solid body, there will be a transfer of heat from the higher-temperature to the lower-temperature region. This heat is said to be

---

[1]The information contained in this chapter, except where noted, can be found in [Kreith and Bohn] and [Holman].

transferred by conduction. The rate of heat transfer due to conduction, q_k, is proportional to the material's *thermal conductivity*, k, the temperature gradient, dT/dx, and the cross-sectional area, A, through which the heat is transferred:

$$q_k = -kA\frac{dT}{dx} \; .$$ (2.16)

The minus sign arises from the second law of thermodynamics, which requires heat to flow in the direction from the higher to the lower temperature (Fourier's Law of Conduction). The heat transfer rate is normally expressed in Watts [W].

In the case of steady-state, one-dimensional heat flow through a plane wall (see Figure 2.4), neither the temperature gradient nor the heat flow vary with time and there is a uniform cross-sectional area along the path of heat flow. If the wall faces are held at T_1 and T_2 with $T_1 > T_2$, and if k is independent of T, after integration Equation 2.16 with $L = \int dx$ simplifies to:

$$q_k = \frac{kA}{L}(T_1 - T_2) = \frac{\Delta T}{L/(kA)} \; .$$ (2.17a)

An analogy can be made between the transfer of heat in a thermal system and the transmission of electricity in an electric circuit under Ohm's law ($I = V/R$). The quantity:

$$\frac{L}{kA} = R_k$$ (2.17b)

is the *thermal resistance* of the wall to conduction. The reciprocal of this quantity is known as the *thermal conductance*, K_k. Using these quantities, the similarities to Ohm's Law become apparent: q_k replaces the current I, $(T_1 - T_2)$ replaces the potential difference U, and R_k replaces the electrical resistance R. This electrical analogy may be taken further to simplify problems involving both series and parallel thermal resistances, as well as other modes of heat transfer.
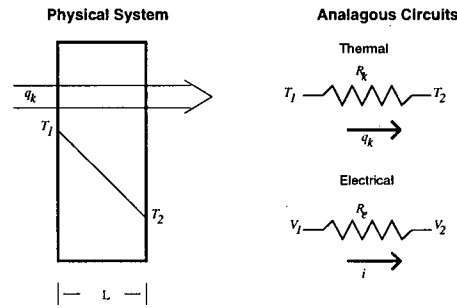
Figure 2.4: Steady-state conduction through a plane wall. The figure demonstrates the temperature distribution within the wall as well as the analogy between thermal and electrical circuits.

2.2.2 Convection

The mode of heat transfer resulting from a fluid or a gas in contact with a solid surface is known as convection. The convection mode of heat transfer is the result of two separate mechanisms operating simultaneously. The first is the energy transfer due to conduction at the fluid-surface interface. The second is the energy transfer due to the macroscopic motion of the fluid particles. This motion can be due to a density gradient caused by temperature variations in the fluid (natural convection), a pressure difference caused by a pump or a fan (forced convection), or a combination of the two.

The heat transfer due to convection is given by the equation (Newton's Law of Cooling):

$$q_c = \bar{h}_c A (T_w - T_\infty) \ , \tag{2.18a}$$

where $\bar{h}_c$ is known as the *convection heat transfer coefficient*, A is the surface area in contact with the fluid, T_w represents the temperature of the solid surface in contact with the fluid, and T_∞ is the bulk temperature of the fluid.

As in conduction, a thermal resistance can be defined for convection:

$$R_c = \frac{1}{\bar{h}_c A} \; .$$

(2.18b)

Again, the reciprocal of this quantity, K_c, represents the thermal conductance.

Exact determination of the convection coefficient $\bar{h}_c$ under forced convection is very difficult due to the complexity of the phenomenon. There are five general methods available for its determination:

1. Dimensional analysis combined with experiments.

2. Exact mathematical solutions of the boundary-layer equations.

3. Numerical analysis.

4. Approximate analyses of the boundary-layer equations by integral methods.

5. Analogy between heat and momentum transfer.

No single method can solve all convection heat transfer problems due to the limitations that restrict each method's scope of applications.

Dimensional Analysis

This method is mathematically simple and is used in a wide range of applications. The method is limited because the results obtained are incomplete and ultimately useless without experimental data. The most serious limitation of dimensional analysis is that it does not give any information about the nature of a phenomenon. In fact, to properly apply the technique, it is necessary to know beforehand what variables influence the phenomenon. A more detailed description of dimensional analysis can be found in chapter 4 of [Kreith and Bohn].

Exact Mathematical Analysis

Exact mathematical analyses require simultaneous solutions of the equations describing the fluid motion and the transfer of energy in the moving fluid. The method requires that the physical mechanisms are understood well enough to be described in mathematical language. This limits the scope of exact solutions because a complete set of equations for the fluid flow and heat transfer mechanisms can be written only for laminar flow, and these equations are still quite complicated. However, solutions have been obtained for simple systems such as flow over a flat plate, an airfoil, or a circular cylinder.

Numerical Analysis

Numerical methods can be used to obtain approximate solutions for the exact equations of motion. The approximate nature of the solutions result from the need to express the field variables, temperature, velocity and pressure, at discreet points in time and space. If the equations are discretized properly, solutions can be made more than sufficiently accurate for engineering applications. There are several advantages to this method. Once a solution procedure has been programmed, solutions can be easily found for different boundary conditions, property variables, etc.

Approximate Analysis of the Boundary Layer

This method uses plausible but simplified equations to describe the velocity and temperature distributions in the boundary layer of the moving fluid. The problem is then analyzed on a macroscopic basis by applying the equation of motion and the energy equation to the bulk of the fluid particles in the boundary layer. This method is relatively simple, yet gives solutions to problems that cannot be treated through exact mathematical analysis. In comparison to conditions where exact solutions are available, the results given by this method agree within engineering accuracy. This

technique can be applied to both turbulent and laminar flow.

Analogy Between Heat and Momentum Transfer

This method is an extremely useful tool for analyzing turbulent systems. Since current knowledge of turbulent-exchange mechanisms is not sufficient to describe the temperature distribution directly, a simplified model must be employed. One widely accepted model dictates that a mixing motion in a direction perpendicular to the mean flow accounts for the transfer of both momentum and energy. This mixing motion is described on a statistical basis by a method similar to that used with gas molecules in the kinetic theory. There is no general agreement that this model corresponds to conditions actually existing in nature; however in practice its use is justified by the fact that experimental results are generally in agreement with analytical predictions based on this model.

In general, whether one applies dimensional analysis or analytic methods, one finds that the heat transfer coefficient, $\bar{h}_c$, can be represented as a function of two or more dimensionless parameters. The convection heat transfer coefficient is represented in dimensionless form by the Nusselt number, which corresponds to the ratio of convection heat transfer to conduction in a fluid layer of thickness L:

$$Nu = \frac{\bar{h}_c L}{k} \, , \tag{2.19a}$$

where L can also be a characteristic length dimension such as the length of a plate, or the diameter of a channel and k is the thermal conductivity of the fluid. $\bar{h}_c$ can be can be solved for through the relation:

$$h_c = \frac{k N_u}{L} \, . \tag{2.19b}$$

The Nusselt number is represented as a function of the Reynolds and Prandtl numbers, *Re* and *Pr*:

$$Nu = f(Re, Pr) \, . \tag{2.19c}$$

The Reynolds number corresponds to the ratio of inertia to viscous forces in the fluid:

$$Re = \frac{U_\infty L}{\nu} = \frac{GD_H}{\mu} \, ,$$ (2.19d)

where in the first term, U_∞ is the free-stream velocity of the fluid, L is a characteristic length dimension and ν is the *kinematic viscosity* of the fluid. In the second term, $G = \frac{\dot{m}}{A}$ is the mass flow per unit area, D_H is the *hydraulic diameter*, a term specific to the geometry of the system, and μ is the *static viscosity* of the working fluid.

The Prandtl number corresponds to the ratio of molecular momentum diffusivity to thermal diffusivity:

$$Pr = \frac{c_p \mu}{k} = \frac{\nu}{\alpha} \, ,$$ (2.19e)

where c_p is the *heat capacity* of the working fluid and α is the *thermal diffusivity* of the fluid.

When the corresponding properties for the fluid have been determined, the relationship described by 2.19c usually appears in the form:

$$Nu = CRe^m Pr^n \, .$$ (2.20)

The constants C, m and n will vary according to the conditions of a specific problem and the nature of the solution.

Convective heat transfer coefficients quoted in reference to the target in Chapters 3 and 5 were calculated using the first method described in this section, dimensional analysis combined with experimental data.

2.2.3 Radiation

The amount of energy leaving the surface of a body as radiation depends on the absolute temperature and the nature of the surface. A perfect radiator, known as a *blackbody*, emits energy from its surface at a rate, q_r:

$$q_r = \sigma A T^4$$ (2.21)

where A is the surface area of the blackbody, T its temperature and σ the *Stefan-Boltzmann constant* $(5.67x10^{-8}\frac{W}{m^2K^4})$. Heat transfer by radiation plays a significant role only at very high temperatures, e. g. in plasma physics. In the temperature range relevant to the investigation presented here, heat transfer by radiation amounts to milliwatts which is negligible compared to other modes of heat transport.

2.2.4 Numerical Analysis

Analytical solutions to heat transfer are generally only possible for relatively simple problems. Where complex geometries and boundary conditions make these solutions impossible, numerical analysis methods can be employed. In these methods, the system geometry is discretized, and solutions are determined at these discrete points within the system. Thus, a difficult differential equation can be simplified into a system of simultaneous algebraic equations.

In describing how such a system of equations would be set up, it is best to start with an example. Figure 2.5 shows a sample two-dimensional problem with a convective boundary condition. Considering the temperature at the node $T_{m,n}$, and applying the fact that at steady-state the total energy entering and leaving the control volume described by the dashed lines surrounding node (m,n) must be equal, one obtains the energy balance equation:

$$-k\Delta y\frac{T_{m,n} - T_{m-1,n}}{\Delta x} - k\frac{\Delta x}{2}\frac{T_{m,n} - T_{m,n+1}}{\Delta y} - k\frac{\Delta x}{2}\frac{T_{m,n} - T_{m,n-1}}{\Delta y} - h_c\Delta y(T_{m,n} - T_\infty) = 0 \ .$$

(2.22)

In the above example, the conductance between nodes (m,n) and $(m-1,n)$ is given by $\frac{k\Delta x}{2\Delta y}$ and is a direct application of Equation 2.17b. In effect, the continuous plate has been replaced by a system of nodes connected by heat-conducting rods. Extrapolating on the above example, a general node of interest i, surrounded by any number of
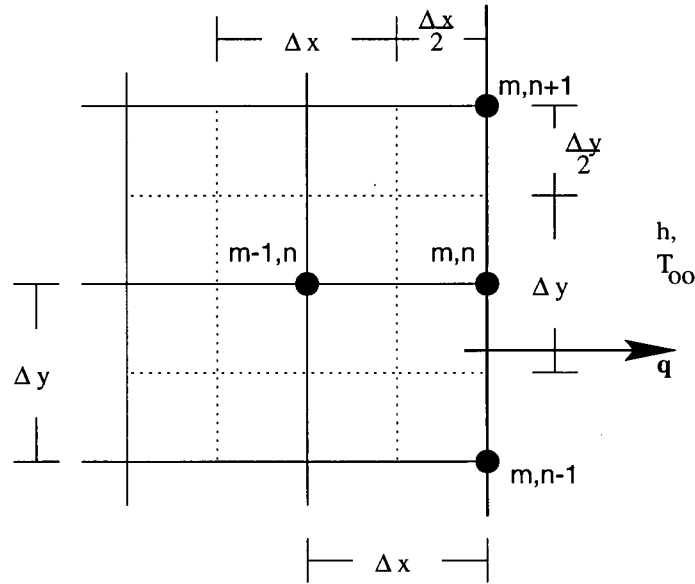
Figure 2.5: Diagram for nomenclature of the nodal equation with a convective boundary condition.

nodes j, with corresponding resistances R_{ij} will satisfy the following equation:

$$\sum_j \frac{T_j - T_i}{R_{ij}} = 0 \ . \tag{2.23a}$$

Solving for $T_{m,n}$ in Equation 2.23a and substituting the the appropriate conductances gives the temperature at any given node T_i:

$$T_i = \frac{\sum_j (\frac{T_j}{R_{ij}})}{\sum_j (\frac{1}{R_{ij}})} = \frac{\sum_j T_j k_{ij}}{\sum_j k_{ij}} \ . \tag{2.23b}$$

Equation 2.23b can be applied to any system of nodes and nodal elements in any desired number of dimensions. There are no restrictions to nodal spacing. In regions where large variations in temperature are expected, nodal spacing can be decreased in order to reduce the error due to discretization; conversely in regions with little temperature variation, the nodal spacing can be increased.

Symmetry in the system being modeled may be used to reduce the number of dimensions, and hence nodes, required to describe a given system. For example, in

a cylindrically symmetrical system, the cylindrical control volume element described by Figure 2.6 may be employed.
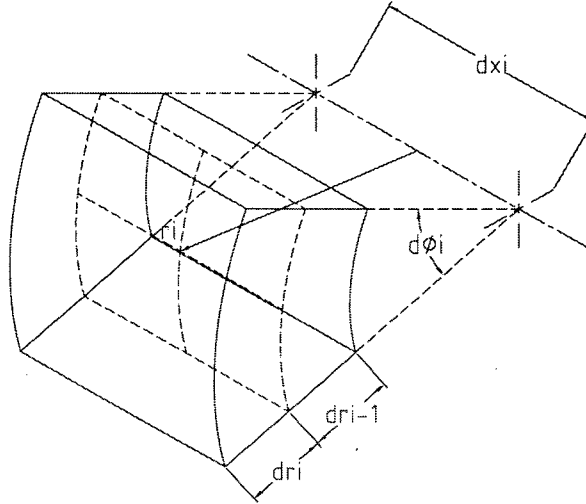
Figure 2.6: A cylindrical control volume element. The node at (r,x,θ) is centered on a control volume defined with variable nodal spacing. The nodal temperature $T_{ri,xi,\theta i}$ is assumed to be constant throughout the entire control volume element.

If there are no differences with respect to the angle θ in the modeled object at a given radius r, the cylindrical control volume element can be centered on a node specified by two coordinates, r and x. Thus, the three dimensional object can be modeled as a two-dimensional system of nodal equations.

Chapter 3

The Target

The target described here was designed for the routine production of ^{18}F as fluoride from enriched $H_2^{18}O$ water via $^{18}O(p,n)^{18}F$ using the EBCO TR-13 cyclotron.

The term 'target' here refers to the material undergoing bombardment as well as the assemblies which are required to contain, isolate, and cool the target material.

The target system consists of six main parts: the collimator; the target window foils; the helium foil-cooling chamber (referred to as the 'helium window'); the target body; the target back wall; and the water cooling insert (referred to as the 'water plug'). A diagram indicating the parts and their order of assembly appears in Figure 3.7 below. Figure A.26 in Appendix A shows how the target is mounted in the target selector of the TR-13 cyclotron.

3.1 The Collimator

The first target component in the path of the proton beam is the collimator. Assembly drawings appear in Figure A.22 of Appendix A. The collimator serves three functions:

1. It collimates the cyclotron beam through its aperture by stopping protons not destined for the target cell, thus minimizing activation of the target selector.

2. It electrically isolates the production target from the rest of the target selector, allowing for an accurate beam current measurement.

23
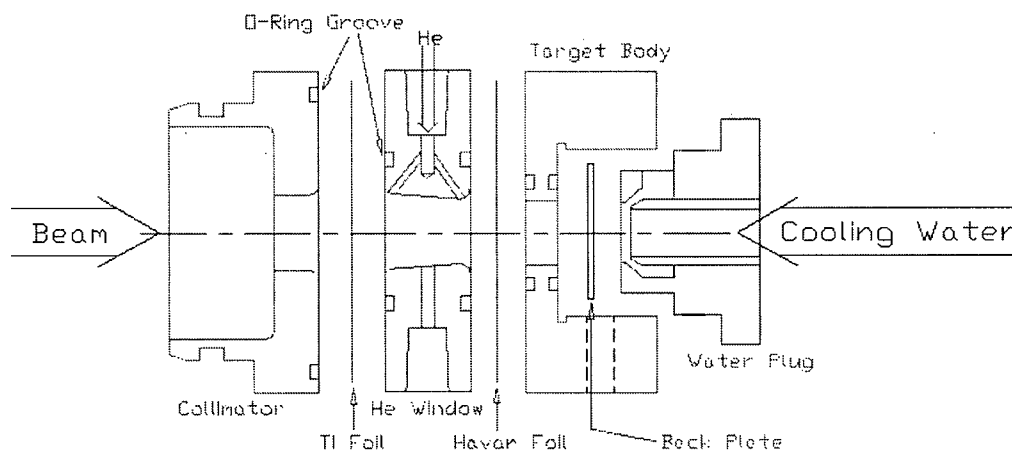
Figure 3.7: Target Components. The diagram shows the order of assembly, as well as the direction of the proton beam and the cooling fluid flow. Where necessary, helium-tight seals between components are achieved with polyurethane o-rings.

3. Along with the helium window, it serves as a mount for the first window foil, compressing the adjacent o-rings and sealing off the helium coolant from the beam line vacuum.

The collimator is milled from a single piece of aluminum, and is anodized to isolate it electrically from the cyclotron. Electrical isolation of components is essential for an accurate beam current reading. No external cooling is provided for the collimator. Adequate cooling results almost entirely through conduction to the helium window chamber.

3.2 The Window Foils

There are two target entrance foils. The first protects the cyclotron vacuum from the helium window coolant, and the second, the target cell foil, seals off the target water in the target cell. The presence of two foils also acts as a safety measure. Should the target cell foil fail, the second foil ensures that the target material and

any radioactivity produced during bombardment will be contained.

3.2.1 Material Choices in Window Foils

In order to minimize energy loss to the traversing proton beam, entrance foils are generally very thin, on the order of 1 to 50 μm [Helus, p.88]. The ideal foil material has high tensile strength, thermal conductivity, melting point, and causes a small energy loss (low Z) to the particle beam passing through. The ideal foil also does not introduce any ions into the target material that would interfere with subsequent chemical syntheses [Votaw(1989)]. Table 3.2.1shows a list of commonly used foil materials and their relevant properties. Havar, titanium, nickel and stainless steel

Material	Atomic Number	Density [g/cm^3]	Melting Point [°C]	Tensile Strength [kpsi]	Thermal Conductivity [W/mK]	dE/dx (@ 10 MeV) [keV/μm]
Be	4	1.85	1283	80	201	6.9
C	6	2.2	>3000	0.6[a]	1960[a]	9.1
Al	13	2.7	660	30	237	9.2
Ti	22	4.5	1668	120	22	13.5
SS	~26	8.02	1427	120	33	22.9
Havar	~27	8.3	1493	250	13	24.2
Ni	28	8.9	1453	120	91	25.4
Cu	29	8.9	1082	30	401	24.2
Nb	41	8.6	2468	50	54	21.2
Mo	42	10.2	2610	80	138	24.4
Rh	45	12.4	1966	110	151	29.4
Ta	73	16.6	2996	35–70	58	30.8
W	74	19.3	3387	500	173	36.3
Pt	78	21.4	1769	20	72	38.6
Ag	47	10.5	962	25–44	429	24.0

[a]Pyrolytic carbon is very anisotropic. Properties depend on the lattice orientation.

Table 3.2: Properties of window foil materials as taken from [Votaw(1989)]. The data for silver [Goodfellow] was added for comparison.

are the most commonly used foils in ^{18}F water targets [Votaw(1989)].

Since the first target foil need only withstand a pressure differential of ~50 *psi* between the helium coolant and the vacuum of the cyclotron chamber, ultimate tensile strength is not as critical as with the target cell foil. For this reason, the material of the first target foil in the current target was chosen to be titanium because of its availability, and because it degrades the cyclotron beam much less than Havar. The target foil thickness used was 25 *μm* (0.01"), which proved more than adequate to withstand the coolant pressure, and also withstood the added pressure resulting from the failure of the inner target foil during testing. According to [Williamson(1966)] this foil degrades the proton beam from 13 MeV to 12.74 *MeV*, thus requiring only ~10.4 *W* of cooling for a 40 *μA* beam.

The material of choice for the target cell foil was Havar. Though it is a poor heat conductor and has a relatively high stopping power, Havar is extremely strong and, almost as importantly, it retains its strength at elevated temperatures and has a high fatigue endurance limit [Hassenzahl(1975)]. Originally, the foil thickness was chosen to be 25 *μm*, but a foil failure during testing prompted the change to a 37 *μm* (0.015") foil. At this thickness, the foil degrades the beam from 12.74 *MeV* to 12.03 *MeV*, necessitating up to 28.4 *W* of cooling in a 40 *μA* beam current.

3.2.2 Foil Strength Calculations

Foil stresses under a given pressure load were determined implicitly using the equations given below [Roark and Young, p. 406,407]:

$$\frac{qa^4}{Et^4} = K_1 \frac{y}{t} + K_2 (\frac{y}{t})^3 \; , \tag{3.24a}$$

$$\frac{\sigma a^2}{Et^2} = K_3 \frac{y}{t} + K_4 (\frac{y}{t})^2 \; , \tag{3.24b}$$

for fixed and held boundary conditions,

$$K_1 = \frac{5.33}{1-v^2} \quad K_2 = \frac{2.6}{1-v^2}$$

$$\text{at center,} \quad K_3 = \frac{2}{1-v} \quad K_4 = 0.976 \tag{3.24c}$$

$$\text{at edge,} \quad K_3 = \frac{4}{1-v^2} \quad K_4 = 0.476$$

where

t = foil thickness,

q = unit load in [MPa] or [psi],

a = supported radius of foil,

E = modulus of elasticity of foil material,

v = Poisson's ratio of foil material,

y = maximum deflection,

σ = maximum stress due to flexure and diaphragm tension combined.

One first solves for y in Equation 3.24a, then obtains the resulting stress from Equation 3.24b.

First Window Foil

The first target foil must be able to withstand the pressure of the helium coolant as well as maintain its integrity should the second foil fail. The target cell pressure should not exceed 34.5 *bar* (500 *psi*) during normal operation. Assuming the target fails at this pressure, and given the volume of the helium cooling chamber immediately in front of the target cell, the first target foil would have to withstand a pressure of ~8.7 *bar* (126 *psi*) for a very brief moment. Results of calculations using Equations 3.24a and 3.24b indicate that failure should not happen in this event. The first foil remained intact after the failure of the target cell foil during testing, supporting the analysis.

Target Cell Foil

As stated in the previous section, the pressure inside the target cell should not exceed 34.5 bar during normal operation. Havar is mostly composed of cobalt, chromium, and nickel[1]; its Poisson ratio is ≈ 0.31 . Using this value of v in Equations 3.24c indicated that a 25 μm foil would fail at the maximum rated target pressure of 34.5 bar. This was confirmed with measurements of pressure during production runs at lower beam currents which caused pressures below the burst limit. In fact, a 25μm foil did fail during a high current test run, and a 37μm foil was then employed. No further failures occurred after the change, even during runs where the pressure limit of 34.5 bar was surpassed for brief periods.

3.3 The Helium Cooling Window

The helium window provides cooling to both target entrance foils. Assembly drawings are shown in Figure A.23 of Appendix A. Cooling of the window foils is critical, both to prevent failure due to weakening from heat stress, and to prolong the life of the foil. Several calculations of beam-heating in entrance foils have been published. Notable are papers by [Steyn(1990)] and [Votaw(1989)] which state conflicting results on the magnitude of forced convection in foil cooling. In [Steyn(1990)] convective heat transfer is estimated to remove 15–25 % of the power deposited in a nickel foil, with the remainder provided by conduction. In [Votaw(1989)] convective heat transfer is estimated to remove >95 % of the deposited power in Havar, titanium and molybdenum foils. Since the thermal conductivity of molybdenum exceeds that of Nickel, it is unlikely that this difference alone accounts for the different estimates. In either case, it is clear that forced convection plays a significant role in the cooling of the target window foils.

---

[1]The composition of Havar is Co 42.5 %, Cr 20 %, Ni 13 %, W 2.8 %, Mo 2 %, Mn 1.6 %, C 2000 ppm, Be 400 ppm, Fe balance [Goodfellow].

3.3.1 Window Coolant

Pressurized helium is used as the window foil coolant here, and is used almost exclusively for this purpose in all small cyclotrons. The reasons for this are threefold:

- While not as good a cooling medium as hydrogen, helium is much safer to use.

- No activation of the helium coolant is possible.

- The beam degradation due to the helium coolant is negligible due to its low Z.

3.3.2 Construction

The helium cooling window used on the target (see Figure A.23) was an older design, first made in 1994, and was used because it was available. It was constructed from a single piece of aluminum and was anodized after machining to isolate it electrically from the cyclotron. The design of the channels forms a system that uses high Reynolds number flow along the foils to increase the heat transfer coefficient.

Helium is supplied to the window through a $\frac{1}{16}$" ($\sim$1.59 *mm*) NPT fitting. The flow is then split into two jets through twin 1 *mm* bore holes, one directed at each window foil. The helium exits through a single 2 *mm* bore hole located 25° away from the entrance holes. From the exit hole the helium leaves the window through another $\frac{1}{16}$" NPT fitting. This arrangement of entrance and and exit fittings is made necessary by the location of the helium supply manifold within the TR-13 target chamber.

3.3.3 Cooling Power

Helium is supplied to the window from the manifold in the target chamber through $\frac{1}{8}$" ($\sim$ 3.13 *mm*) polyurethane tubing at a flow rate $\approx$100 $\frac{L}{min}$, corresponding to a mass flow rate of $1.7 \cdot 10^{-3} \frac{m^3}{s}$. Once it is split through the twin jets, the Reynolds number of the resulting helium jets is $\approx$ 4,700.

Calculation of Convective Heat Transfer Coefficient

The forced convective heat transfer coefficient along the window foils is determined from Equations 2.19b and 2.20. For long circular ducts of diameter D an empirical fit to experimental data results in the Dittius-Boelter formulation of 2.20:

$$h_c = 0.023 \frac{k}{D} (Re)^{0.8} (Pr)^{0.3} .$$ (3.25)

Since turbulence requires about 10 to 15 duct lengths to develop and about the same to die out [Kreith and Bohn], this formula should give reliable information as to the amount of convective cooling to expect from the window. The forced convective heat transfer coefficient along the window is thus calculated to be $>850 \frac{W}{m^2 K}$. On the 1 *cm* diameter beam spot, this corresponds to a cooling power of $\approx 6.6 \frac{W}{K}$.

The first and second foils receive 10.4 *W* and 24.8 *W* due to beam heating in a 40 μA beam, respectively. This results in heating power densities of 13.2 and 31.6 $\frac{W}{cm^2}$. If the foils reach a conservative temperature of $\simeq 350$ °*C*, the cooling power density provided by the helium would be approximately 30 $\frac{W}{cm^2}$. Barring any gross nonuniformities in the cooling power distribution, the cooling delivered by the Helium window should be more than adequate to dissipate the energy deposited in the window foils by the proton beam.

3.4 The Target Body

The target body serves as the enclosure for the target chamber and as the mounting point for all of the major target components. Detailed design drawings are located in Figure A.24 in Appendix A. A simplified diagram of the the target body appears in Figure 3.8 :
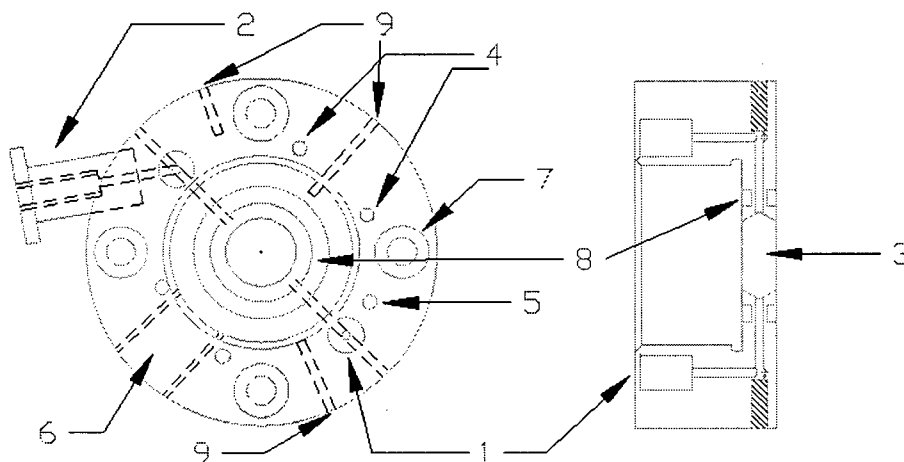
Figure 3.8: The Target Body. Simplified plan and side views are provided. The indicated components are as follows: 1. Valve stem threads; 2. Pressure transducer mount; 3. Target chamber, which houses the $H_2{}^{18}O$. The arrow also denotes the direction of the proton beam. 4. Water plug mounting threads; 5. Current lead screw hole; 6. Cooling water exit; 7. Main holes through which mounting bolts pass. These bolts thread into the collimator and hold the major components of the target together; 8. O-ring grooves; 9. Thermocouple mounting holes.

3.4.1 Construction

The target body is constructed of titanium in two parts: the main body, and the pressure transducer mount. Titanium was chosen as the target material because it is very inert and does not introduce contaminants that will irreversibly bind the ^{18}F ions. The pressure transducer mount is press fit into the main body and welded. An Entran model EPZM-10*-500G pressure transducer was fitted to this mount during assembly. This pressure transducer has a maximum rated capacity of 500 psi (34.5 *bar*).

The target cell is 'V' shaped (see Figure 3.8) in an attempt to minimize the possibility of trapping any gas, which could lead to inordinate pressure rises during bombardment. The volume of the target cell is $\sim$500 μL. The target was designed to

be operated as a closed volume, and so no reflux volume was provided for the target water. Polyurethane o-rings on both sides of the cell provide a seal against the back wall and with the Havar foil.

Three holes, aligned with the mid point of the target cell and concentric with the center of the cell, serve as thermocouple mounts for a trio of $\frac{1}{16}$" shielded thermocouples. The holes were drilled to depths of 14, 11 and 7 *mm* (11, 14, and 18 *mm* from the center of the target cell, respectively), allowing the thermocouples to provide a temperature profile of the target body during its operation (see details 9 in Figure 3.8).

3.5 The Back Wall of the Target Chamber

The back wall of the target chamber separates the target material from the cooling water. The seal is provided by a polyurethane o-ring (see detail 8 in Figure 3.8).

3.5.1 Construction

The back wall is a 21 *mm* diameter disk composed of 0.25 μm-thick platinum bonded to 0.5 *mm* of silver. The bonding was achieved by casting the silver onto the platinum using a wax-replacement method.

The platinum was bonded to the silver to separate the silver from the target water. While silver does not bind the [^{18}F]fluoride into inert compounds, it does form deposits within the target chamber after prolonged use, necessitating the removal and cleaning of the target [Berridge(1986)]. Platinum was chosen as the separation material for two reasons: 1. It is inert and does not bind ^{18}F into inert compounds [DeJesus(1986)]. 2. It is easily bonded to silver.

A foil like the thin window separating the target cell from the helium coolant was not used since deflection caused by the direct impact of the cooling water would

decrease the volume of the target cell during the filling procedure. Once the proton beam was applied to the target, the resulting pressure rise would force the foil to deflect in the opposite direction. The target cell would no longer be completely filled with $H_2{}^{18}O$, resulting in lower yields caused by the irradiation of steam.

3.5.2 Back Wall Strength Calculation

The back wall must withstand the same pressure as the second window foil, that is 34.5 *bar* (500 *psi*). The stress in the back wall under this load was calculated using Equations 3.26a to 3.26e [Roark and Young, p.362]. These sets of equations are valid only for cases where $y_c \leq \frac{t}{2}$. Otherwise, Equations 3.24a and 3.24b must be employed.

$$D = \frac{Et^3}{12(1-v^2)} \qquad (3.26a)$$

$$y_c = -\frac{qa^4}{64D} \qquad (3.26b)$$

$$M_c = \frac{qa^2(1+v)}{16} \qquad (3.26c)$$

$$M_{ra} = -\frac{qa^2}{8} \qquad (3.26d)$$

$$\sigma = \frac{6M}{t^2} \qquad (3.26e)$$

The parameter D is first calcualated, followed by the maximum plate deflection, y_c, the bending moments M_c and M_{ra}, and finally the material stress, σ. Calculations indicate that the silver plate should hold, with a maximum deflection of 0.034 *mm*.

3.5.3 Thermal Conductivity of the Back Wall

The advantage of using silver in the construction of the back wall is its extremely high thermal conductivity (see Table 3.2.1). The extremely thin platinum foil adds

Definitions for Equations 3.26a to 3.26e:

t =   thickness of the plate,
ν =   Poisson ratio of the material,
D =   plate constant,
y_c =   maximum plate deflection,
$M_{c,ra}$ =   bending moment in the plate at the center and the outside radius,
σ =   stress in the plate with the given bending moment.

very little to the overall thermal resistance. Using Equation 2.17b, it was determined that the thermal resistance of the back wall due to conduction is the same as that offered by a 25 μm Havar foil.

3.6 The Water Plug

The water plug serves to direct cooling to the back wall of the target cell and around the interior perimeter of the target body. A detailed design drawing is located in Figure A.25 in Appendix A. Figure 3.9 shows a simplified cross-section showing the plug as it is mounted within the target body.

3.6.1 Construction

The plug is machined in two parts: the main fitting and the nozzle. The main fitting is machined from a single piece of aluminum and serves as a mount for the nozzle and the cooling water supply. The plug is connected to the rest of the target using four 3 mm bolts threaded into the target body. The nozzle is machined from stainless steel and is threaded into the main fitting. It is held in place by the application of locktite glue to its threads.

Cooling water is supplied to the water plug through a $\frac{1}{4}$" polyurethane tube. A positionable male elbow Swagelock fitting (model SS-400-2-4ST) is used to connect the supply line to the plug. Water is then directed to the back wall of the target cell
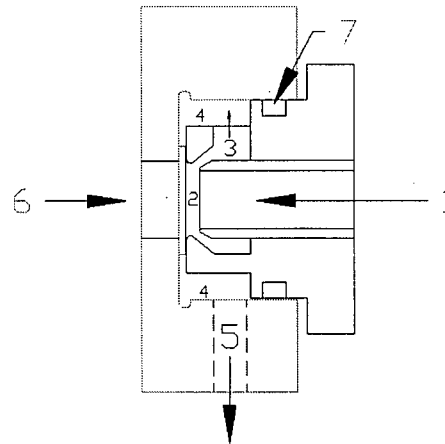
Figure 3.9: The Water Plug, here shown as it is inserted in the target body. Components are as follows: 1. Cooling water entrance to nozzle; 2. Cooling water strikes back wall; 3. Exit from water plug; 4. The interior perimeter of the target body; 5. Cooling water exit through target body; 6. Direction of proton beam; 7. O-ring seal.

through a 5 *mm* bore nozzle. Once the water strikes the back wall at high speed, it is directed back through the water plug on the outside of the nozzle where it is then directed out to the interior perimeter of the target body, diverging in two paths as it circulates, then exiting the target. In order to ensure that the cooling water circulates within the target perimeter, it is important that the exit from the water plug be oriented directly opposite to the cooling water exit located on the target body.

3.6.2 Convective Heat Transfer Coefficients

Cooling is provided to the target by the water plug in two main regions, indicated by (2) and (4) in Figure 3.9.

Region (2)

The coolant flow conditions in region (2) are unique and have not been solved analytically. Therefore, two separate semi-empirical solutions were applied to the problem

in order to come up with a reasonable estimate of the heat transfer coefficient along the coolant side of the back wall.

In order to determine the heat transfer coefficient, the Reynolds number, *Re*, of the cooling water flow through the nozzle must first be determined. Using Equation 2.19d, the Reynolds number of the cooling water flow was determined to be ~8,700.

The first solution method employed follows experminental results of non-circular cross sections in liquids compiled by Jakob [Holman]. Among these results are empirical solutions to the heat transfer coefficient along non-circular cylinders, including a flat plate, in free-stream flow. The equation for the convective heat transfer coefficient, $\bar{h}_c$, provided by the cooling water along the back wall of the target cell is given by the formula [Holman, p. 306]:

$$\bar{h}_c = 0.228 \frac{k}{D} R_e^{0.731} Pr^{\frac{1}{3}} , \qquad (3.27)$$

where the length parameter D is the internal diameter of the cooling water supply line, in this case 4 mm. From this equation, it was found that $\bar{h}_c \simeq 39,000 \frac{W}{m^2 K}$. If the nozzle diameter of 5 mm is used as the length parameter in the determination of the Reynolds number of the flow and the resulting heat transfer coefficient, $\bar{h}_c$ turned out to be $\simeq 34,000 \frac{W}{m^2 K}$. These values appeared rather large, so a second method was used to verify the results.

The second method employed approximates the flow in region (2) as channel flow over a flat plate; in effect, the origin of the flow was assumed to be in the center of the plate, with the flow radiating outwards with a film thickness equal to the gap between the nozzle and the back wall of the target cell. The Reynolds number for this flow condition was determined using Equation 2.19d, with the hydraulic diameter determined in the following manner:

$$D_H = 4 \cdot \frac{\text{flow cross-section}}{\text{wetted perimeter}} = \frac{4 \pi D s}{\pi D} , \qquad (3.28)$$

where $s = 1$ *mm* is the distance between the nozzle and the back wall and D is the diameter of the back wall of the target cell. The resulting $D_H = 4$ *mm* gives a Reynolds number $Re \simeq 8,700$. The Dittius-Boelter formulation of Equation 2.20 (Equation 3.25) can once again be employed, this time substituting the fluid properties of water for those of helium. This approach also results in a convective heat transfer coefficient of $\sim 34,000$ $\frac{W}{m^2 K}$ along the back wall.

Because the condtitions along the back wall represent a non-ideal case, the lower value $\bar{h}_c = 34,000$ $\frac{W}{m^2 K}$ was used as the convective heat transfer coefficient on the cooling water side of the back wall.

Region (4)

The coolant flow conditions in Region (4) presented a simpler case in determining the convective heat transfer coefficient along the interior perimeter of the target body. The channel in Region (4) presents a square cross-section to the flow, so Equation 3.28 was again employed to determine the proper length parameter to use in the Reynolds number and heat transfer coefficient calculations.

The channel dimensions are 8.7 x 3.4 *mm*, which results in an hydraulic diameter D_H of 4.8 *mm*. Substituting this value into Equations 2.19d and 2.20, noting that the water flow splits in two in this channel, results in a heat transfer coeffient $\bar{h}_c \simeq$ 5,000 $\frac{W}{m^2 K}$.

3.7 Assembly and Installation

The target is assembled from the front. The collimator is placed face-down on the table, followed by the o-ring and the first target foil. The helium window and the target body are aligned so that the helium entrance and exits and the pressure transducer mount are oriented in the same direction. This orientation is made necessary by the

limited space available within the target selector of the TR-13. Four 5 *mm* bolts fitted through mounting holes on the target body and the helium window are threaded into the collimator. The bolts are then tightned, providing helium-tight seals at all interfaces. The back wall and the water plug are then mounted, followed by the cooling water supply fitting (Swagelock model SS-400-2-4ST). The target fill and vent valves (General Valve #9-152-901) are mounted on valve stems and oriented in line with the cooling water supply fitting. The three thermocouples are then inserted into their mounting holes in the target body and fixed to prevent their movement during installation. The target is then ready to be mounted in the target selector (Figure A.26).

For mounting, the collimator is pressed into the target assembly mount, with care taken to ensure that the target fill and vent valves are oriented vertically to minimize the possibility of trapping gas within the target cell. The selector is then evacuated, sealing the collimator against the target mount and holding the target tightly in place. The fill and vent lines are connected to the valves. The bolus detector which indicates the complete filling of the target is positioned on the vent line as close to the vent valve as possible. The helium and water coolant supply and return lines are then connected, followed by the valve power leads and the target current lead. Two more thermocouples were placed in-line with the cooling water at the entrance and the exit to the target with Swagelock 'T' fittings. A cooling water supply separate from that used by other targets in the cyclotron was installed. This was done for two reasons: it prevented contamination of the cooling water supply in the event of failure of the back wall of the target cell, and it allowed for the use of an in-line meter in measuring the cooling water flow.

3.8 Target Operation

The target was installed with the permission of the TRIUMF PET group in the EBCO/TRIUMF TR-13 cyclotron located in the TRIUMF facility in Vancouver, BC. It has since been

operated within the guidelines established by the PET group.

3.8.1 Loading and Unloading

Originally, the target was filled and emptied from the PET chemical laboratory located 25 m from the cyclotron. Since May 1997, it has been filled through approximately 4 m of $\frac{1}{16}$" tubing from a station located next to the cyclotron. The target is still emptied to the laboratory through approximately 30 m of $\frac{1}{16}$" polypropylene tubing.

Figure 3.10 shows a schematic representation of the unit for remotely filling and emptying the target.

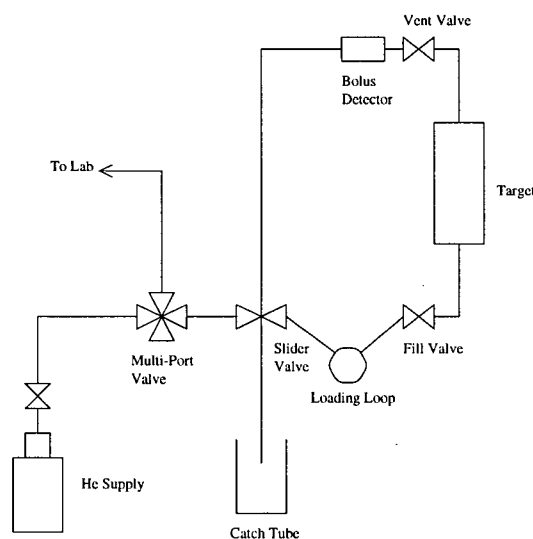Figure 3.10: Schematic representation of the unit for remotely filling and emptying the H$_2{}^{18}$O target.

Loading

The target is loaded by filling a looped section of $\frac{1}{16}$" polypropylene tubing with $\sim$1 ml of water using a syringe, being careful to ensure that the water stays intact as a single bolus. The multiport valve is turned to the 'load' position where it provides

pressure to the fill line connected to the target. The slider valve is set in the 'load' position, meaning pressure will be directed on the target fill line. The loop is then connected in line with the fill line of the target. A computer control program which opens and closes the target valves is then executed. Both valves remain open as a helium pressure of 5–10 psi pushes the water into the target and through the top valve. Once the bolus detector senses that the water bolus has reached the vent line after having filled the target chamber completely, the computer program immediately shuts both target valves. The target is then ready for bombardment.

Emptying

The target is emptied through the same line with which it is filled. The slider valve is moved to direct helium pressure to the vent line at the top of the target. The multi-port valve is positioned to return the bolus to the PET chemistry lab, some 25 *m* away. The same computer program used to load the target is then used to open the target valves, allowing the helium pressure to force the water bolus back through the fill line, through the multiport valve and on to the chemistry lab. Approximately 10–25 *psi* of helium pressure is required to empty the target in this manner.

3.8.2 Target Bombardment

During bombardment several target parameters were monitored: cyclotron beam current; target pressure; cooling water inlet and outlet temperatures; three temperatures within the target body. Care was taken to ensure that the target pressure never exceeded 500 *psi* (34.5 *bar*). In practise, this meant that current would be increased until the target pressure exceeded ~420 *psi*, since the pressure rise increases rapidly with increasing current.

Chapter 4

Irradiation Experiments

The experiments referred to in this chapter were conducted during the winter and spring of 1997, and again in the fall. Measurements taken included product suitability and yield data as well as target operational data for various beam currents. A chemical synthesis was also performed to verify the purity of product and the viability of the target in a ^{18}F production role.

4.1 Product Data

Tests involving the production of ^{18}F from enriched $H_2{}^{18}O$ were conducted on February 14, 1997 and during October 1997. Tests focussed on the purity of the fluoride product and determination of product yields for various currents.

4.1.1 Product Suitability

The $^{18}F^-$ product suitability was confirmed on May 30, 1997 with the synthesis of labelled setoperone using the standard synthesis method employed in the TRIUMF PET laboratory.

A 30 *min* irradiation at an average current of 10 μA produced approximately 175 *mCi* of radiofluoride at EOB. The ^{18}F product was used to synthesize 35.3 *mCi* of 476 $\frac{Ci}{mmol}$ setoperone. The specific radioactivity lies well within acceptable standards as practiced at the TRIUMF facility, confirming that the $^{18}F^-$ product appears in a

form suitable for chemical syntheses. This, and the fact that the radioactivity in the setoperone produced was more than sufficient for a patient dose [Huser] confirms that the target is suitable for the production of ^{18}F –labelled radiopharmaceuticals.

4.1.2 Product Yield

Runs to determine the efficiency of the target production of ^{18}F were conducted during the fall of 1997. A graph of the results appears in Figure 4.11.
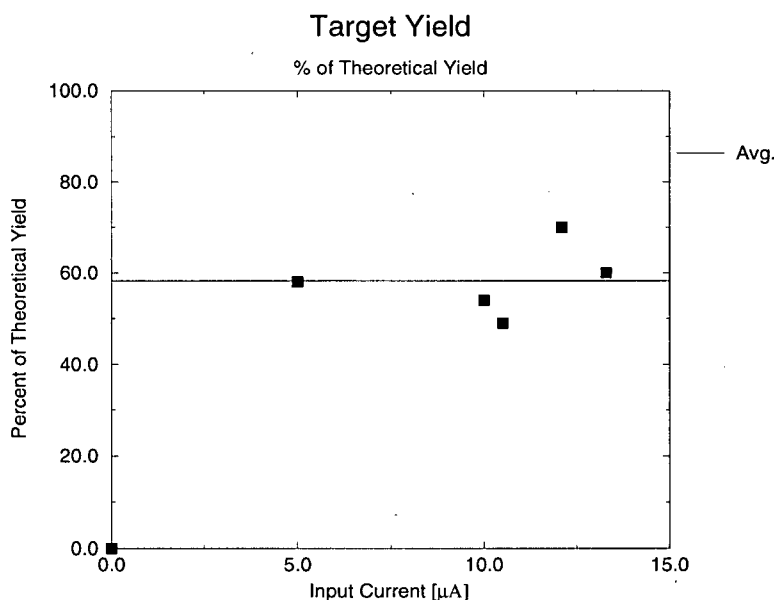
Figure 4.11: Percentage of EOB theoretical yield for 12 *MeV* protons

Yields were calculated as a percentage of the theoretical thick target yield based on the measured thick target saturation yields according to T. J. Ruth and A. P. Wolf [Ruth(1979)].

As is evident from the graph, there is no apparent pattern to the ^{18}F yields with increasing current. Unfortunately, higher current runs were not achieved during these particular tests, making it impossible to determine whether there would be a fall-off

in yield due to a density reduction in the beam path as current increased beyond 15 μA. The average production yield achieved over the course of 5 runs averaging 10 μA was 58.2 % of the theoretical thick target yield.

4.2 Operational Data

Operation parameters measured during target runs included the current on the target, target pressure, the temperatures within the target body, and the inlet and outlet temperatures of the cooling water. The results of these measurements are examined in the following sections.

4.2.1 Target Pressure Data

Target performance in terms of current capability proved to be highly variable, as illustrated in Figure 4.12. The reasons for this extreme variability are not known. One factor to note is the trend towards poor target performance as the number of runs on the target increased.

4.2.2 Target Temperature Data

Target temperature data was gathered in the course of all experiments. Data in this section is taken from those experiments used in the modeling of the target.

Cooling Water Temperatures

The temperature of the cooling water was measured with shielded $\frac{1}{8}$" T-type thermocouples installed in-line with the water supply at both the inlet and the outlet to the target during its operation. Temperature measurements were conducted with a hand-held Fluke meter with an accuracy of ± 0.1 °C. Temperatures were measured

Target Pressure Vs Input Current
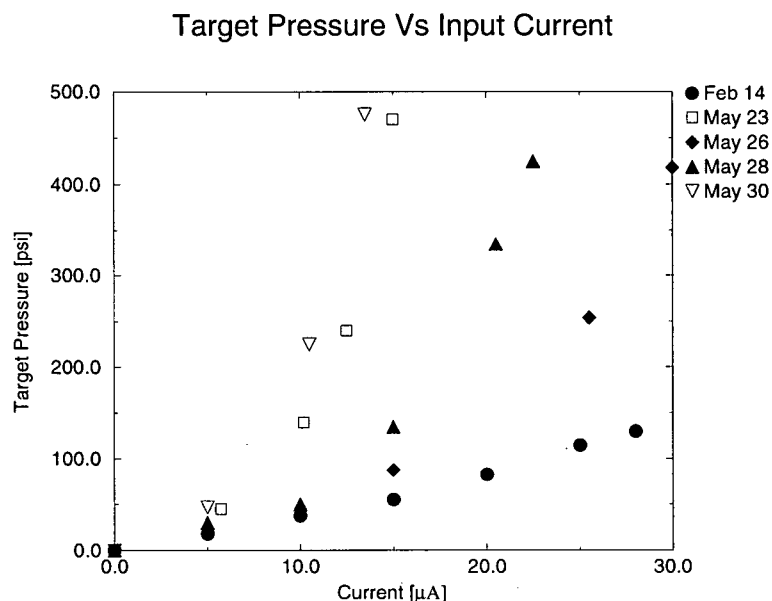
Figure 4.12: Target pressure during test runs conducted during 1997. The data covers runs performed both on natural and 98 % ^{18}O enriched water. Note that runs where the highest currents were reached exhibit the lowest pressures at a given current.

over a range of beam currents in order to confirm that as suspected, the great majority of the energy deposited in the target is removed by the water coolant. The results of the temperature measurements appear in Table 4.2.2.

The high error associated with the removed heat is due to the nature of the measuring equipment. With temperature measurements accurate to ± 0.1 °C, and cooling water flow rates accurate to 0.006 $\frac{L}{s}$, the minimum error in the heat transfer calculation from the target was ~ 41 W. One error not taken into account was that the cooling water was in a closed loop, and was constantly rising in temperature as the experiment was being conducted. Since input and output temperature measurements could not be performed at the same time, this could have contributed a small amount to the measurement errors.

Current [μA]	Power [W]	ΔT [°C]	$\dot{m}C_p\Delta$T [W]	$\delta\dot{m}C_p\Delta$T [W]	% $\frac{\dot{m}C_p\Delta T}{\text{Power}}$	δ% %	# of Meas. #
5	60	2	109	42	182	70	5
10	120	5	134	43	112	36	3
10.5	126	5	175	42	139	33	1
12	144	6	161	41	112	28	1
12.5	150	6	194	43	129	29	1
13	156	6	161	41	103	26	1
13.5	162	6	215	43	133	27	1
15	180	7	211	46	117	26	3
20	240	15	285	51	119	21	1
20.5	246	16	249	45	101	18	1
22.5	270	17	305	49	113	18	1
25	300	19	285	51	95	17	1
28	336	21	380	55	113	16	1
30	360	23	388	54	108	15	1

Table 4.3: A summary of the cooling water temperature measurements. The values in the column labelled "ΔT" indicate the measured temperature rise in the cooling water after it passed through the target. The next column shows the calculated energy input required to raise the cooling water by that amount. The next column then shows the error in this energy calculation. The values in the column labelled "%" indicate the ratio of the energy removed from the target as compared to the actual energy input to the target given by $E_p \cdot I$. These values should all be 100, if all of the heat input to the target were removed in the cooling water. All measurements do agree with this value within error, except for the 5, 10.5, and 13.5 μA values. These discrepancies appear to be due to errors in measurement, since they indicate more heat was removed from the target than was deposited by the proton beam.

Target Body Temperatures

Temperatures within the target body were measured at radii of 11, 14 and 18 mm from the center of the target cell, as described in Section 3.4.1. Measurements were conducted with shielded $\frac{1}{16}$" T-type thermocouples and a hand held Fluke meter accurate to ± 0.1 °C.

Temperature variation in the target body proved to be negligible. In fact, contrary to expectations, temperatures at the outer two radii proved to be consistently higher than in the innermost point. This is believed to be due to conduction from the

beam-heated collimator and helium window to the target body. Only the innermost temperature measurement of the target body was used in calculations involving the target model for two reasons:

1. *The innermost point is closest to the target water, which was much higher in temperature than the rest of the target body.* It is therefore believed that the temperature at this point would have been more greatly affected by heat transfer from the target cell than other points in the target body.

2. *The innermost radius measurement was close to the helium-cooled region of the window.* Since the helium window is partially cooled by the helium flowing within the window chamber, it is reasonable to assume this would provide some cooling to the inner radii of the helium window body, resulting in less heat transfer to the target in this region.

The heat transfer model of the target body is discussed further in Chapter 5.

Chapter 5

The Target Model

A simple heat transfer model of the target body using control volume analysis was developed on a Quattro Pro Version 7 spreadsheet. None of the functions used were restricted to this particular piece of software. As long as the spreadsheet uses the current cell values in subsequent iterative rounds, any modern spreadsheet program would work as well. The program can iterate the spreadsheet up to 255 times before a subsequent iteration round must be manually initiated. It takes about 5 minutes over approximately 10,000 iterations on a Pentium 120 computer to converge to a solution after starting with blank cell values.

5.1 Model Overview

The model described here was developed in order to achieve better understanding of the heat transfer between the target water and the surrounding body. Specifically, the magnitude of the heat transfer coefficient between the target water and the target cell wall was of interest, since it determines how much heat energy can be removed from the target. The model was developed to be as simple as possible, considering itself with only those factors believed to be most prevalent to the removal of energy from the target cell.

The model was not designed to completely describe all of the paths for heat flow from the target body. Instead, it was developed in an attempt to quantify the heat

transfer coefficient between the target water and the walls of the target cell in order to obtain an estimate of its magnitude. By understanding the modes of heat transfer from the target cell and their relative magnitudes, the largest resistances to heat transfer can be identified and then this knowledge can be applied in future designs.

5.1.1 Model Assumptions

Several assumptions were made to simplify the problem for a spreadsheet solution.

Target Water Temperature

The temperature of the target water was assumed to be at the saturated liquid temperature for the measured operating pressure, and uniform throughout the target cell.

The target water temperature is probably not completely uniform at any given instant, since most of the proton beam energy is deposited near the proton stopping distance in water [Heselius(1989)]. However, the absence of fluctuation in temperatures throughout the target body as well as in inlet and outlet cooling water during operation indicate that there is a time-averaged constant target temperature during steady-state operation.

The choice of the saturated liquid temperature at the operating pressure is easily justified. At a given operating current, the pressure in the target is relatively constant, and since the volume of the target is fixed, this indicates a constant target water temperature. In [Steinbach(1990)] the temperature of the target water in an open $H_2^{18}O$ target was measured. The target water temperature was found to be constant at $100\ ^\circ C$, the saturated liquid temperature for water at atmospheric pressure. This measurement was developed one step further with measurements taken on a $H_2^{18}O$ target at the Forschungszentrum Karlsruhe GmbH. Here, pressure and temperature measurements were taken in a closed target over a wide variety of beam

currents. Again, the target water temperature at a given operating pressure was found to be the saturated liquid water temperature [Becker(1997)]. A graph showing how vapour pressure varies with water temperature is shown in Figure 5.13.
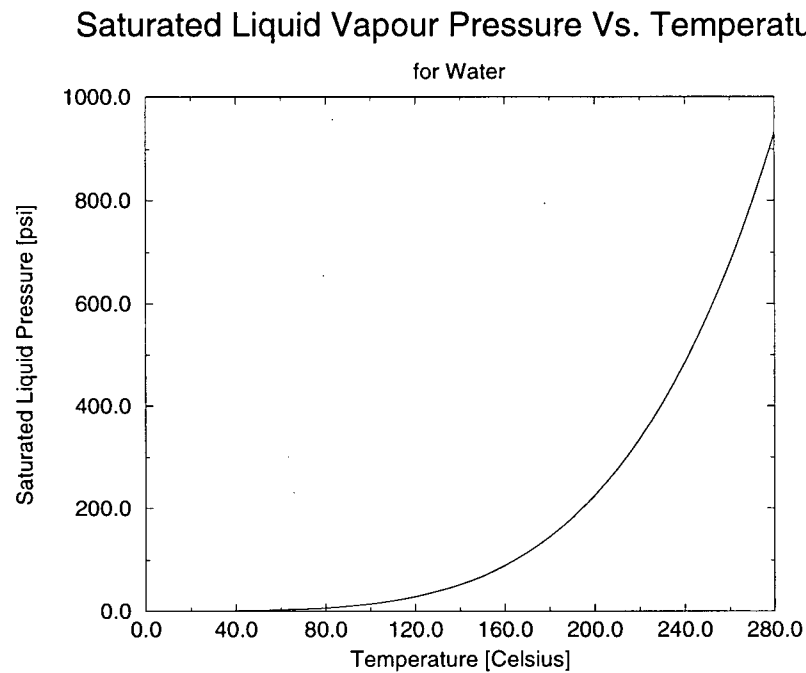
Saturated Liquid Vapour Pressure Vs. Temperature
for Water

Figure 5.13: The saturated liquid vapour pressure Vs. temperature for water.

Simplification of the Target Body Geometry

In order to facilitate the modeling of the heat transfer using a spreadsheet, two important and related simplifications were necessary.

The target model geometry had to be simplified. Discontinuities such as the bolt holes for mounting target components, the threaded holes to which the fill and vent lines were mounted and the thermocouple mounting holes themselves were not incorporated into the model. The 'V'-shaped groove within the target cell was also not represented. Instead the target cell was modeled as being a smooth cylinder 10 mm

in diameter. Given that these account for a very small fraction of the total volume of the target body, and that only the bulk modes of heat transfer were of concern, the assumptions seem reasonable.

The target was assumed to have equal temperatures at equal radii within the target body. This follows directly from the previous assumption of a uniform temperature within the target cell, and the simplification of the geometry.

These assumptions allow the simplification of the three dimensional heat transfer within the target body to a two-dimensional problem, where only the radius and the horizontal axis are considered.

Boundary Conditions

Only conductive and convective boundary conditions were considered. The heat loss due to radiation was considered negligible, since it is an order of magnitude less than even free convective heat loss at the relatively low target body temperatures recorded during operation [Kreith and Bohn, p. 560].

The target body was also considered an isolated unit. Contact heat transfer between these two components was not considered.

Havar Entrance Foil

Heat transfer through the Havar entrance foil to the target cell was not considered. Preliminary estimations of the heat transfer coefficient within the target cell indicated that it would be more than two orders of magnitude greater than the convective heat transfer coefficient of the Helium coolant on the surface of the Havar foil. This assumption was verified once the model was completed. The elimination of this surface from consideration greatly simplified the model since energy deposition within the target foil no longer had to be considered.

Outer Surface

A free convective heat transfer coefficient of 10 $\frac{W}{m^2 K}$ was assumed for the outer surface of the target. This parameter is not critical to the prediction of the model. It can be increased or decreased by a factor of 10 with little impact on the results; the figure used is a well within the range of most free convection, and is commonly used in assumptions of a free convection heat transfer coefficient [Kreith and Bohn, p.509]. It is included since the outer surface of the target body is not insulated, and since it was easily incorporated into the model.

5.2   Implementation of the Target Model

The model was developed using the numerical technique of control volume analysis described in Section 2.2.4, using cylindrical control volumes as illustrated in Figure 2.6. Variable node spacing was employed in order to reduce the total number of nodes, while retaining sufficient accuracy in regions where the temperature gradient was the largest. A screen shot of the spreadsheet model appears in Figure 5.14.

5.2.1   The Spreadsheet Model

The model uses two parameters derived from individual actual targets run as input: the target water temperature, obtained from the saturated liquid water temperature at the operating pressure; and the measured temperature of the target body at a radius of 11 mm from the center of the target cell and a distance of 2.4 mm from the front of the target body. The target cell temperature and the heat transfer coefficient between the target water and the walls of the target cell (U_{cell} in Figure 5.14) are set, and the system is iterated until the nodal temperatures become stable. U_{cell} is varied until the nodal temperature at the 11 mm radius is equal to that measured during

Target Heat Transfer Model

h back	hair	Ucell						
34000	0.034	10	1E-05	50000	0.05	0.005	22	0.022
[W/m2K]	[W/mmK]	[W/mm2K]	[W/mm2K]	[W/m2K]	[W/mm2K]	[W/mm2K]	[W/mK]	[W/mmK]

All dimensions in mm.

Target Pressure   130 [psi]

	Surface Avg dT	9.66	[C]	%Total
	Q body	72.81	[W]	22.28
	Q back	253.96	[W]	77.72
	Q total	326.77	[W]	
	Q actual	336	[W]	(@ 28 uA)

These areas are for the first set of dX data.
The rest get scaled.

dT	7.81	8.52	10.22	11.37	11.71	11.26	10.04	8.34	7.64
dX		0.6							

[mm2] Ar+	Ar-	As	dR
19.04	18.85	1.57	0.1
19.42	19.04	3.20	
19.79	19.42	3.27	
20.17	19.79	3.33	
20.55	20.17	3.39	
20.92	20.55	3.46	
21.30	20.92	3.52	
21.68	21.30	3.58	
22.05	21.68	3.64	
22.43	22.05	3.71	
22.81	22.43	3.77	
24.88	22.81	21.86	1
28.65	24.88	44.61	
32.42	28.65	50.89	
35.25	32.42	42.29	0.5
38.08	35.25	45.83	1
42.22	38.08	73.61	1.2
46.75	42.22	88.97	0.1
49.20	46.75	51.97	
49.57	49.20	8.23	
53.16	49.57	81.33	1.8
60.32	53.16	179.67	
67.86	60.32	213.63	2
75.40	67.86	238.76	
82.94	75.40	263.89	
90.48	82.94	289.03	
94.25	90.48	150.80	

Nodal temperature grid (R-axis rows vs. X-axis columns); x-coordinate labels: 0, 0.6, 1.2, 1.8, 2.4, 3, 3.6, 4.2, 4.8, 5.4, 6, 6.6, 7.2, 7.8, 8.4, 8.7, and upper labels 0.3, 1, 5, 10, 15, 20.

Surface row: 179.8 179.8 179.8 179.8 179.8 179.8 179.8 179.8 179.8 179.8

R	0	0.6	1.2	1.8	2.4	3	3.6	4.2	4.8
5	172.0	171.3	169.6	168.4	168.1	168.5	169.8	171.5	172.2
5.1	170.2	169.4	167.3	165.9	165.4	166.0	167.5	169.6	170.5
5.2	168.6	167.5	165.0	163.3	162.8	163.5	165.3	167.8	168.8
5.3	167.0	165.8	162.7	160.8	160.2	161.0	163.0	166.1	167.3
5.4	165.6	164.1	160.5	158.3	157.6	158.5	160.8	164.5	165.9
5.6	164.2	162.5	158.2	155.8	155.1	156.0	158.6	162.9	164.6
5.7	162.9	161.0	156.0	153.2	152.5	153.5	156.4	161.5	163.3
5.8	161.8	159.7	153.7	150.7	149.9	151.0	154.2	160.1	162.2
6.8	160.8	158.4	151.3	148.2	147.3	148.5	152.0	158.9	161.3
6.9	160.0	157.3	148.9	145.6	144.7	145.9	149.7	157.9	160.5
6	159.3	156.4	146.4	143.0	142.1	143.4	147.3	157.0	159.8
6.1	158.8	155.7	143.8	140.4	139.4	140.8	144.8	156.3	159.3
7.1			115.9	112.8	112.0	113.0	116.2		
8.1			83.3	83.3	83.2	83.2			
9.1			54.6	57.2	57.8	56.8	53.9		
9.6			45.4	47.2	47.6	46.6	44.3	41.0	38.5
10.6	41.4	42.3	40.6	40.9	40.8	40.0	38.5	36.7	34.8
11.8	39.8	40.0	36.2	36.0	35.6	34.8	33.8	32.5	31.1
13	36.3	36.3	32.8	32.5	32.0	30.5	30.5	29.4	28.0
13.1	33.1	33.0	32.6	32.3	31.8	31.4	30.3	29.0	27.7
13.2	32.8	32.7	32.3	32.0	31.5	30.9	30.0	29.0	27.7
15	32.6	32.5	28.9	28.7	28.3	27.9	27.4	26.8	26.1
17	29.1	29.1	26.6	26.4	26.2	25.9	25.6	25.2	24.8
19	26.7	26.7	25.1	25.0	24.9	24.7	24.5	24.5	23.9
21	25.2	25.2	24.3	24.2	24.1	23.9	23.8	23.6	23.4
23	24.3	24.3	23.8	23.7	23.7	23.5	23.4	23.2	23.1
	23.9	23.8	23.7	23.6	23.5	23.4	23.3	23.1	23.0
26	23.7	23.7	20	20	20	20	20	20	20

Right-hand water-channel block (columns 5.4, 6, 6.6, 7.2, 7.8, 8.4, 8.7, 9, 10, 15, 20):

T@11mm 39.04 C
39

5.4	6	6.6	7.2	7.8	8.4	8.7	9	10	15	20
20	20	20	20	20	20					
20	20	20	20	20	20					
20	20	20	20	20	20					
26.0	24.7	23.8	23.1	22.5	22.0	21.5	21.3	21.0	20.7	20.3
26.1	24.8	23.9	23.1	22.5	22.0	21.6	21.3	21.0	20.7	20.3
26.1	24.9	23.9	23.2	22.6	22.1	21.7	21.3	21.0	20.7	20.3
25.3	24.7	24.0	23.4	22.9	22.4	21.9	21.5	21.1	20.7	20.3
24.4	24.0	23.5	23.1	22.7	22.2	21.8	21.4	21.0	20.7	20.3
23.6	23.9	23.0	22.7	22.3	22.0	21.7	21.3	21.0	20.7	20.3
23.1	22.9	22.6	22.4	22.1	21.8	21.5	21.2	20.9	20.6	20.3
22.9	22.7	22.4	22.2	21.9	21.7	21.4	21.2	20.9	20.6	20.3
22.8	22.6	22.4	22.1	21.9	21.7	21.4	21.1	20.9	20.6	20.3
20	20	20	20	20	20	20	20	20	20	20

Figure 5.14: The target model as implemented on the Quattro Pro spreadsheet. Nodal coordinates can be interpreted from the column marked **R** and the row labelled **X**. The numbers within the cells represent the nodal temperatures of the target body. The columns labelled **Ar+**, **Ar-**, **As** and **dR**, indicate the surface areas between the nodes in the positive and negative radial directions, in the x-direction and the radial nodal spacing, respectively. The numbers along the row labelled **dX** indicate the horizontal nodal spacing. The shaded area below the x-coordinates represents the target cell water temperature. Dark shaded areas represent insulated surfaces. The lightly shaded rectangular area to the right-center of the figure represents the cooling water as it passes through the channel formed between the interior of the target body and the water plug. The results of the model appear in the top-right corner of the spreadsheet.

the target run[1]. The heat transfer from the target water to the target body is summed up along the nodes adjacent to the target cell. Heat transfer through the back wall of the target is computed analytically using the concepts outlined in Section 2.2. The two values are then added and compared to the actual input power during the target run.

The Spreadsheet Layout

The model was developed using the same concepts used in Section 2.2.4. Referring to Figure 5.14, it is clear that the model is not represented to scale, however the shape of the target body is apparent in the figure. The spreadsheet model is constructed in several layers or pages. The first page produces the nodal temperatures and computes the heat transferred from the target cell. Subsequent pages are used to calculate the conductances within the spreadsheet model.

Nodal temperatures are determined using Equation 2.23a. Conductances for each node are computed using the conduction and convection equations (Equations 2.17b and 2.18b) where appropriate.

Sources for error can be identified. While the front face of the target body is assumed to be insulated in the target model, it is in contact with the Helium window, which is in contact with the uncooled collimator. Therefore, some part of the power deposited in the collimator and the helium window by the beam will end up in the target body. Since the beam profile from the TR-13 is Gaussian as confirmed by visual inspection, the amount of beam current striking the collimator and the helium window should be negligible compared to the current deposited in the target.

---

[1]Since the temperature of the cooling water varies with time and ambient temperature, the nodal temperature at 11 mm was matched *relative* to the temperature of the cooling water. That is, if the measured temperature at 11 *mm* was 40 °C and the cooling water input temperature was 25 °C, the nodal temperature would have been matched to 35 °C, that is 15 °C above the cooling water temperature indicated in the target model.

5.3 Model Results

The results of the model can be interpreted in two ways: how closely it agreed with
test results; and what the results can tell us about how heat is transferred from the
target cell.

5.3.1 Accuracy of the Model

A comparison of the heat transfer prediction from the model with the actual power
input to the target appears in Figure 5.15. From the figure, it is apparent that fairly
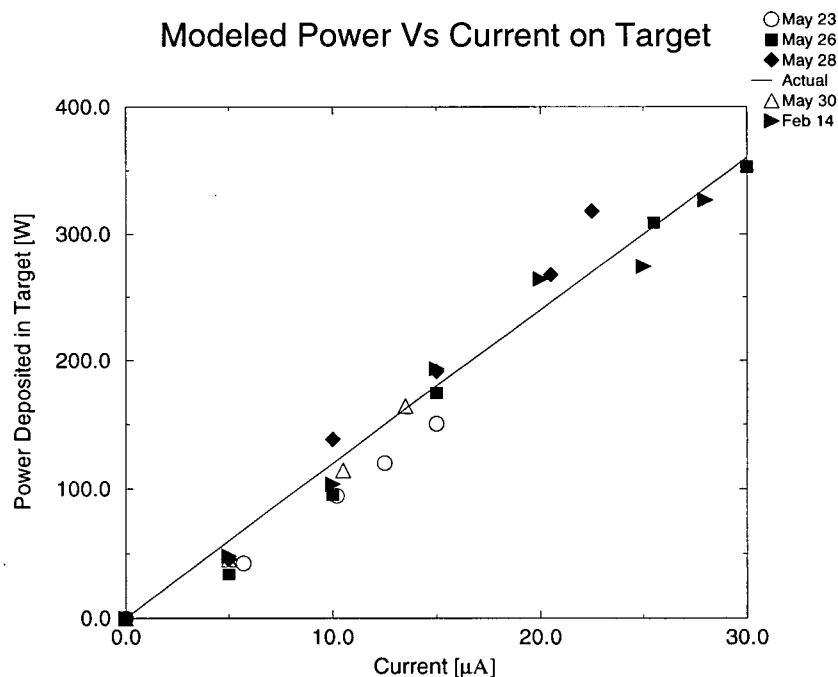

Figure 5.15: Results of modeled target runs. The figure shows the results of modeled target
runs vs. input current for these runs. The solid line representing the actual beam energy
deposited on target for a given beam current is shown for comparison.

good agreement exists between the target model predictions and the actual power in-
put during the modeled runs. Though the data for higher power runs are limited, the

agreement improves between the model and actual input power as the input power to the target increases. Improving agreement with increasing power is represented

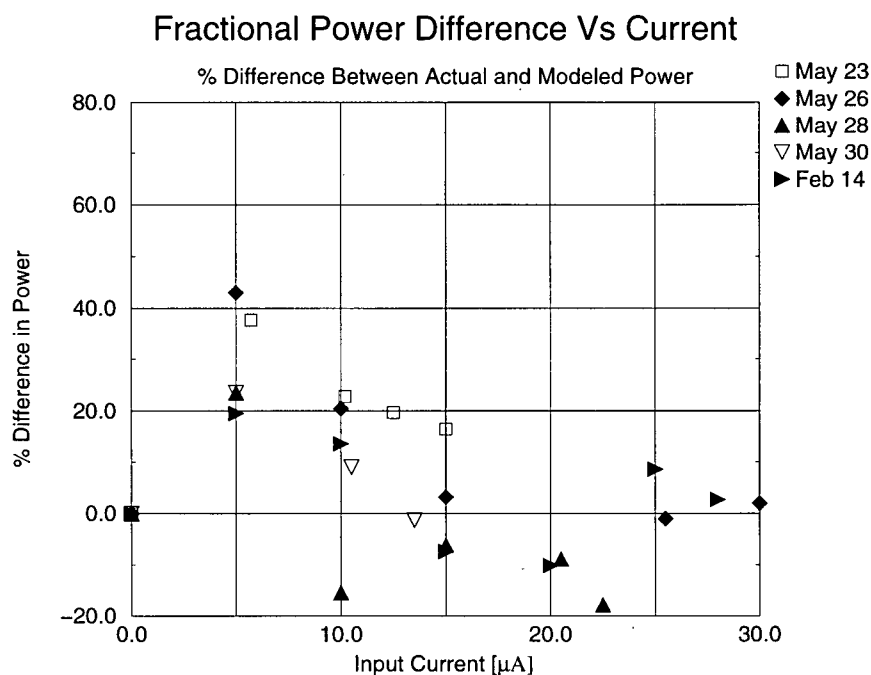## Fractional Power Difference Vs Current

Figure 5.16: The fractional power difference vs. current for each modeled run. Underpredictions in power input result in positive differentials on the graph.

graphically in Figure 5.16, which clearly shows that the model predicted the input power within ±18 % for input currents above 15 μA. Agreement is within ±23 % for currents above 10 μA. It appears that agreement was best for those test runs where higher current was achieved, as represented by the filled data points. In general, one can see that the model underpredicts power input to the target, though overpredictions are clearly present. Since a small portion of the beam current strikes the collimator or the window and thus does not reach the target cell, and the measured current is delivered to the whole target and not merely the target cell, an accurate model would be expected to underpredict the power deposited on the target water.

There are several possible reasons why the model agreement improves with runs

having higher power input:

1. *Systematic errors associated with the model simplifications become more prevalent with lower power input to the model.* If the power input to the target cell is 60 *W* (a 5 μAbeam current at 12 *MeV*), a variation of 20 *W* with respect to the model amounts to more than a 33 % difference. In contrast, if the power input during the target run was 240 *W* (a 20 μAbeam current at 12 *MeV*) a variation of 20 *W* with respect to the model results in a difference of only 8 %. Therefore small sources of heat transport not considered due to simplifications become less significant as the modeled power increases.

2. *The saturated liquid water temperature variation with pressure decreases with increasing pressure.* During operation, the target pressure variation Δp, lies within a within a range of values from ±3 or ±5 *psi* to as much as ±20 *psi* as pressure rises above 400 *psi*. Since target pressures were recorded as an estimated average of the pressure transducer readout, some judgemental error was inevitable. Figure 5.13 clearly shows a very large variation in water temperature over the lower end of the pressure scale. The saturated liquid water temperature at 500 psi is just over 240 °*C*. By the time the temperature scale has reached half way to this point, or 50 % of its maximum value, the target pressure has only reached 29psi, or just under 6 % its value at 240 °*C*. The decrease in target water temperature variation with increasing target pressure therefore makes errors in pressure measurement less critical, even though the Δp in the target pressure measurements increase with pressure. Figure 5.17 below shows some support for this analysis.

3. *The model is not representative of the heat transfer through the target. Agreement with increasing power may be coincidental since it is based on limited data.* The model is based on sound physical concepts that are well tested. Figure 5.15

clearly shows a direct correlation between the model predictions and the current input to the runs on which they were based. It is true that data have been recorded for only three runs with currents above 15 μA. However, the model data below 15 μAfrom these three runs falls well within the ranges for the other model predictions, and even at low beam currents model agreement is best with data gathered from these particular runs.
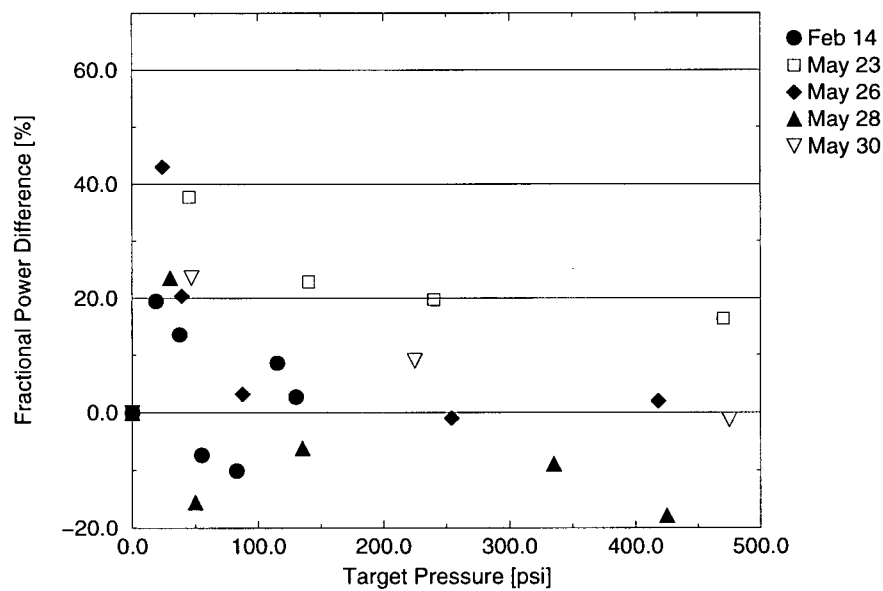

Figure 5.17: Fractional power difference in modeled power input compared to pressure measured on target. The figure shows decreasing variation as pressure increases. As before, the data for runs where the highest current on the target were achieved are showing the least variation.

5.3.2 Data Analysis

Variation of the internal heat transfer coefficient U_{cell} with input current is shown in Figure 5.18. In the graph U_{cell} varies greatly with individual currents but in general

increases with current. Within individual runs, the trend to greater internal heat transfer coefficients with increasing current is apparent. This trend is expected. As current input (thus beam power) to the target cell increases the U_{cell} must increase to compensate, since the external heat transfer coefficients and resistances remain fixed.
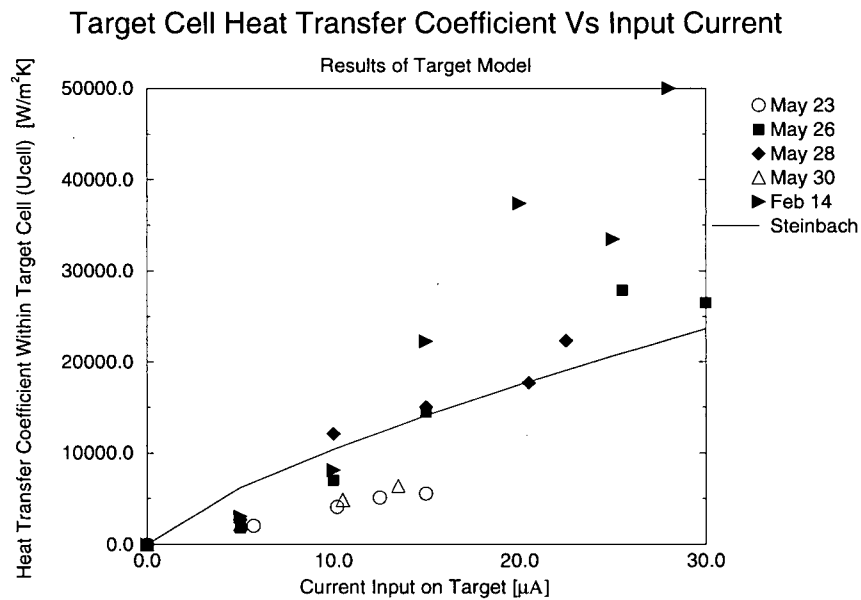
Target Cell Heat Transfer Coefficient Vs Input Current

Figure 5.18: Model results of target cell heat transfer coefficients compared to input current. The necessary rise in the internal heat transfer coefficient with input current is very apparent. As before, the data with solid markers indicate runs where higher current was achieved. The solid line indicates theoretical predictions from an equation appearing in [Steinbach(1990)].

[Steinbach(1990)] provides a relation between the absorbed power density and the heat transfer coefficient due to boiling water; saturated liquid water is by definition at the boiling point. This relation appears in Equation 5.29, where $q_{wabsorbed}$ is the power density on target in $\frac{W}{cm^2}$.

$$U_{cell} = 0.154 q_{wabsorbed}^{0.75} \qquad (5.29)$$

A comparison with the model results shows relatively good agreement at currents

below 15 μA. At currents above this value, the model is in fair agreement with theory, excepting the February 14 data. For this data, the model steadily overpredicts the value of U_{cell} when compared to Equation 5.29, with the maximum discrepancy of a factor of 2.5 occurring at 28 μA. However, some encouragement for the accuracy of the model can be inferred, since the values of U_{cell} predicted by the equation and the theory are well within the same order of magnitude. It could be that factors other than boiling such as convective forces due to target water motion are contributing to U_{cell} in this case.

Another interesting observation here is that runs where higher currents were achieved consistently exhibit higher internal heat transfer coefficients. Again, this is to be expected, since in order to hold the target pressure down the target water temperature must be kept lower, and in the same target, this can only arise through higher internal heat transfer coefficients. This is portrayed graphically in Figure 5.19 which shows the variation of U_{cell} with target water temperature. As expected, for higher current runs U_{cell} is larger through all temperature ranges, and is dramatically larger as the target water temperature rises above 125 $^\circ C$.

5.3.3 Interpretation of Data

Though results of the target model are often highly variable, this is most likely due to the high variability in the target performance during the runs on which the model was based. One possible reason for this variability may be incomplete filling of the target cell with water. Figure 5.19 provides some insight to this.

Since higher current runs are exhibiting a higher U_{cell} than in runs where a lower maximum current was reached, something must be interfering with the heat transfer in the lower current runs. One possible source of this interference may be an incomplete filling of the target. If the target cell is not completely filled with water, there is less target water in contact with the interior surface of the target cell. Some
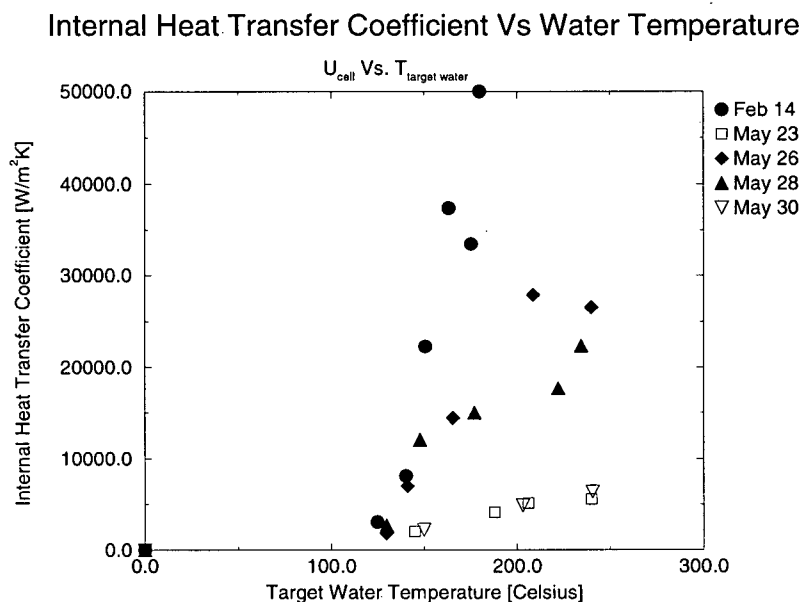
Figure 5.19: Model results of target cell heat transfer coefficients compared to target water temperature.

of the water may boil off, adding to vapour pressure within the target. In general, gas-surface interfaces offer resistances to heat flow an order of magnitude or two higher than fluid-surface interfaces [Holman, p.509]. So in an incomplete fill, the surface area within the cell available for cooling the target water is decreased which in effect results in a lower heat transfer coefficient between the target water and the walls of the target cell. This is reflected in the low determination of U_{cell} for runs with maximum currents below 20 μA.

Another insight provided by the model is the determination of the paths for heat flow. The model provides information as to how much heat is transferred through the back wall of the target cell and how much leaves the target cell through the body of the target. These are shown in Figures 5.20 and 5.21. At currents below 5 μA, just over half of the heat is leaving the target water radially through the body of the target cell, with the remainder passing through the back wall of target cell. This situation

reverses itself with increasing current, reaching a peak of $\sim$75 % through the back wall at currents above 25 μA. This happens despite the fact that the internal radial area of the target cell is $\sim$151 mm^2 while the area of the back wall of the cell is 78.5 mm^2—about half as much.

When one examines the thermal resistances, the reasons become clear. At a current of 5μAU_{cell} is approximately 2000 $\frac{W}{m^2 K}$ as predicted by the model. Using Equation 2.18b, this results in a thermal resistance of 3.3 $\frac{K}{W}$ radially between the target water and the body of the target cell. Using the same equation, the thermal resistance between the target water and the back wall is 6.3 $\frac{K}{W}$, or about twice as much. In comparison, the thermal resistance due to conduction offered by the back wall itself is given by Equation 2.17b and comes to 0.02 $\frac{K}{W}$ and the thermal resistance on the cooling water side of the back wall, again given by Equation 2.18b, is 0.37 $\frac{K}{W}$. Thus, the thermal resistance between the target water and the interior of the target cell is dominating the heat transfer from the target water. One would therefore expect just under twice as much heat to be passing through the target body as through the back wall under these conditions. This is reflected in Figures 5.21 and 5.20, where at 5 μAwe see that approximately 60 % of the heat energy is transferred through the target cell wall and 40 % is passing through the back wall.

In contrast, at 25 μAa typical U_{cell} is approximately 27,000 $\frac{W}{m^2 K}$ as given by the target model. This results in target cell thermal resistances of 0.24 $\frac{K}{W}$ radially and 0.47 $\frac{K}{W}$ along the back wall. These are in the same order as the thermal resistance between the cooling water and the back wall of the target cell. Therefore the comparative resistances offered by the target body and the back wall of the target cell will come into play. Since the target body is constructed of titanium which has a thermal conductivity approximately $\frac{1}{15}$ that of silver (the material of the back wall), and the path through the target body to the cooling water is several millimeters, while the path through the back wall is only 0.5 mm, the path of least resistance to heat flow

is through the back wall. This is again reflected in Figures 5.21 and 5.20, where we see that ~75% of the heat energy is transferred through the back wall of the target cell at currents above 25 μA.

One thing that must be noted is that even at its lowest, the thermal resistances between the target water and the back wall, and between the cooling water and the back wall are still an order of magnitude larger than the thermal resistance offered by the material in the back wall itself. Thus, the greatest source of thermal resistance to heat transfer from the target water occurs along the fluid-surface interfaces, both within the target cell, and between the cooling water and target surfaces.

This information can be used in future target designs. Since a major source of resistance is between the target water and the target cell, a future design should try to maximize the surface area in contact with the target water. A design incorporating ridges or fins within the target cell is one way to increase the available surface area, and the same can be done on the surfaces exposed to the cooling water. Or, if such a design is impractical to manufacture, a design exposing the the radial walls of the target cell could be implemented, thus exploiting the greater surface area available for cooling along this dimension. The current target concentrates the cooling power of the water coolant along the back wall, and does little to offer cooling to the radial surface of the target cell. By forcing a path of several millimeters through the titanium body, where it eventually finds the cooling water path along the inside of the target body, at a much lower velocity, and thus a much lower heat transfer coefficient, the largest source of available surface area for cooling is wasted.

One criticism of the target model is that it is restricted to the target in question. This is partly true, however the concepts used in the model can still be applied to compare competing model designs. In the absence of temperature data, Equation 5.29 can be applied to provide a conservative value for the target cell heat transfer coefficient, since in general, U_{cell} as predicted by this equation are less than those

predicted by the spreadsheet model. The target water temperature can be once again be assumed to be the saturated liquid water temperature at the rated operating pressure of the target design. Meaningful comparisons between target designs can thus be achieved using software available to almost any physics lab, without the purchase price and learning curve associated with dedicated finite element analysis software.
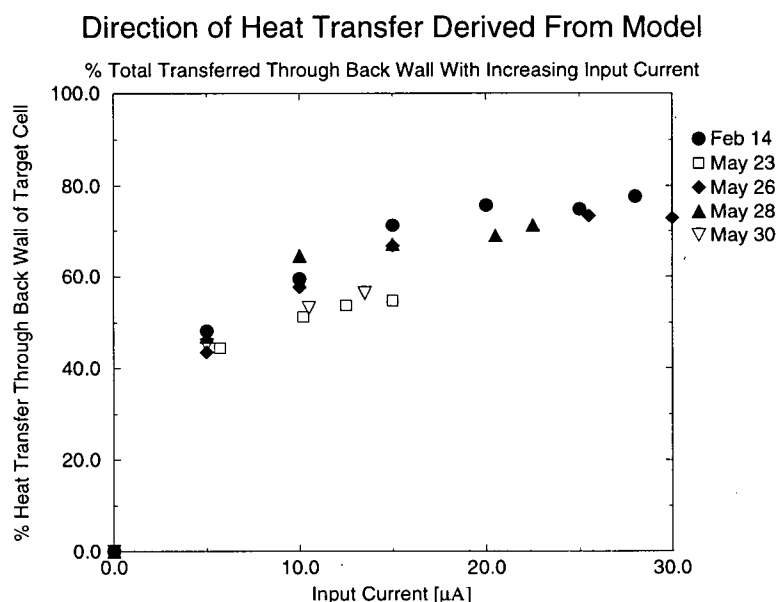
Figure 5.20: Model results of target cell heat transfer through the back wall of the target as compared to input current.
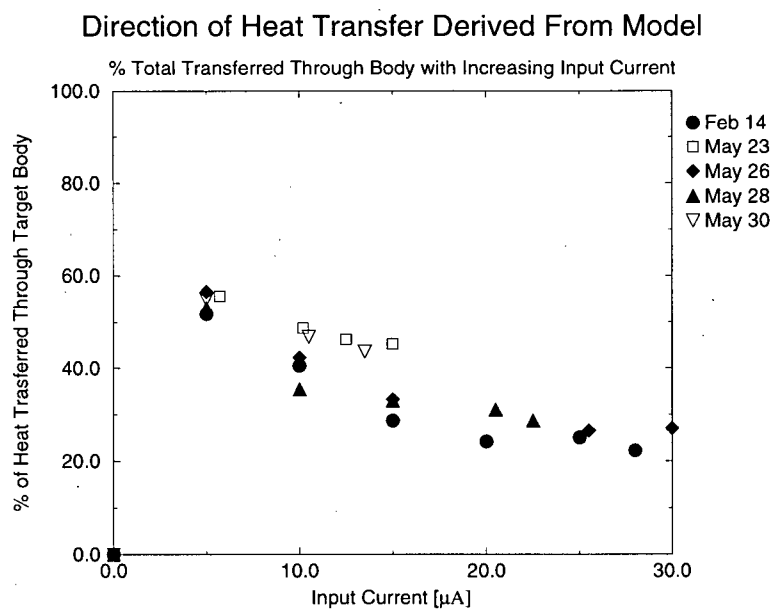
Figure 5.21: Model results of target cell heat transfer through the body of the target as compared to input current. This is, of course, the complement of Figure 5.20.

Chapter 6

Conclusion

An target for the production of ^{18}F -fluoride through the irradiation of $H_2^{18}O$ was built and tested. The target was found to produce ^{18}F -fluoride of adequate quantity and quality for the production of radiopharmaceuticals.

A spreadsheet-based heat two-parameter heat transfer model of the target was developed to identify the major modes of heat transfer from the target cell, and thus largest resistances to the removal of heat from the target. The model was in good agreement with data taken during target operation. Using the model, it was found that the largest resistances to heat transfer from the water target occur along the fluid-surface interfaces, both within the target cell, and along the cooling surfaces in the target. Improved target designs should take this into account, and attempt to maximize the surface area available for cooling the target cell.

Bibliography

[Becker(1997)] Dirk Becker, DKFZ. Private Communication. *WTTC 1997.* Heidelberg.

[Berridge(1986)] M.S. Berridge, T.J. Tewson *Recommendations for Effects of Target Design on the Production and Utilization of [F-18]-Fluoride Production from [O-18]-Water.* J. Lab. Comp. Radiopharm. **23** No. 10-12 1177 (1986).

[Bubb(1981)] Ernest Bubb et al. *Heat Extraction from Targets in High Current Electron Beams.* Nucl. Instr. Meth. **203** 101 (1982).

[DeJesus(1986)] O.T. DeJesus et al. *[^{18}F]Fluoride from a small Cyclotron for the Routine Synthesis of [^{18}F]2-fluoro-2-deoxy-D-glucose.* Appl. Radiat. Isot. **37** No. 5 397 (1986).

[Guillaume(1991)] Marcel Guillaume et al. *Reccomendations for Fluorine-18 Production.* Appl. Radiat. Isot. **42** No. 8 749 (1991).

[Hassenzahl(1975)] W.V. Hassenzahl and W.H. Gray, Los Alamos report LA-5833-MS (1975).

[Helus] Frank Helus *Radionuclides Production, Volume II.* CRC Press, Boca Raton (1983).

[Heselius(1989)] S.J. Heselius et al. *A Diagnostic Study of Proton-beam Irradiated Water Targets.* Appl. Radiat. Isot. **40** No. 8 663 (1989).

[Holman] J.P. Holman *Heat Transfer, Seventh Edition.* McGraw-Hill, Toronto (1990).

[Huser] Joe Huser, Chemist, TRIUMF PET Laboratory. Private Communication during synthesis of setoperone. Vancouver, B.C. Canada May 1997.

[Krane] K.S. Krane *Introductory Nuclear Physics.* John Wiley and Sons, Toronto (1988).

[Kreith and Bohn] F. Kreith, M.S. Bohn *Principles of Heat Transfer, Fifth Edition.* West Publishing Company, St. Paul (1993).

[Keller] K.A. Keller, J. Lange, H. Muenzel *Q-Values and Excitation Functions for Nuclear Reactions,* Landolt-Boernstein New Series Group I, Vol. 5, Springer (1973).

[Goodfellow] *Catalog of Metals, Alloys, Compounds, Ceramics and Poymers.* Goodfellow Corporation, Berwyn, PA. 189 (1994).

[Roark and Young] *Formulas for Stress and Strain, fifth ed.* McGraw-Hill, Montreal (1975).

[Roberts(1995)] A. Roberts et al. *A High Power Target for the Production of [^{18}F]Fluoride.* Nucl. Inst. Meth. Phys. Res. B **99** 797 (1995).

[Ruth(1979)] T.J. Ruth, A.P. Wolf *Absolute Cross Sections for the Production of ^{18}F via the ^{18}O(p,n)^{18}F Reaction.* Radiochimica Acta. **26** 21 (1979).

[Solin(1988)] O. Solin et al.*Production of ^{18}F from Water Targets.* Appl. Radiat. Isot. **39** No. 10 1056 (1988).

[Steinbach(1990)] J. Steinbach et al. *Temperature Course in Small Volume [^{18}O]Water Targets for [^{18}F]F$^-$ Production.* Appl. Rad. Isot. **41** No. 8 753 (1990).

[Steyn(1990)] Steyn et al. *Helium Cooling of a Double-Foil Window for External Cyclotron Beams.* Nucl. Inst. Meth. Phys. Res. A **292** 35 (1990).

[Votaw(1989)] J.R. Votaw, R.J. Nickles *A Theoretical Description of the Beam Induced Heating of Accelerator Target Foils.* Nucl. Inst. and Meth. **281** 216 (1989).

[Williamson(1966)] C.F. Williamson, J.-P. Boujot, J. Picarde*Tables of Range and Stopping Power of Chemical Elements for Charged Particles of Energy 0.05 to 500 MeV.* Rapport CEA-R 3042 (1966).

[Wojciechowski(1987)] Peter W. Wojciechowski et al. *A Semi-Quantitative Approach to the Design, Analysis and Operation of a Gas Target System.* Appl. Radiat. Isot. **39** No. 5 429 (1987).

Appendix A

Design Drawings

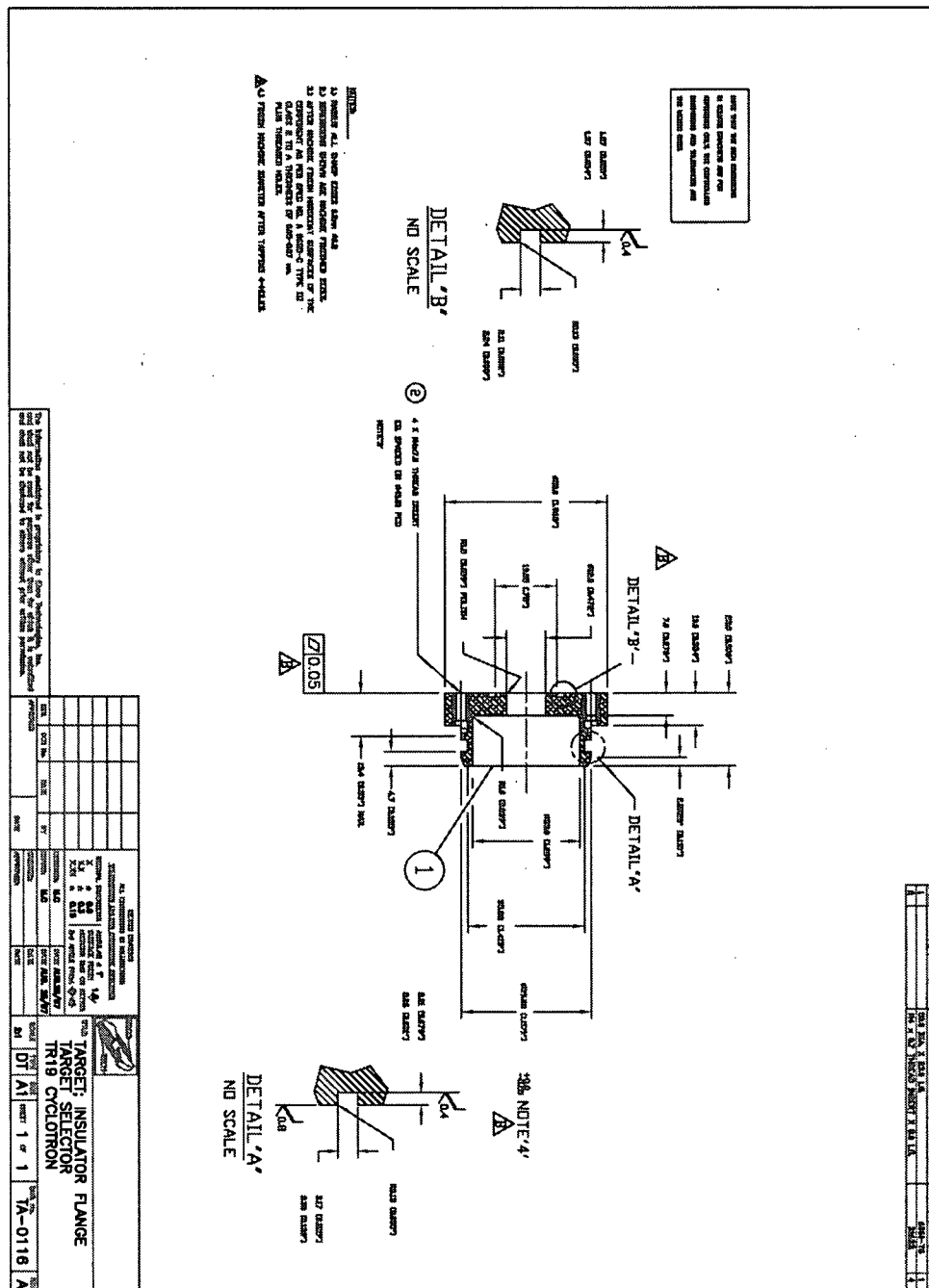This section contains the design drawings of the various target components, as they were delievered to the machine shop.
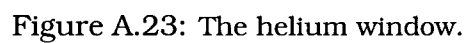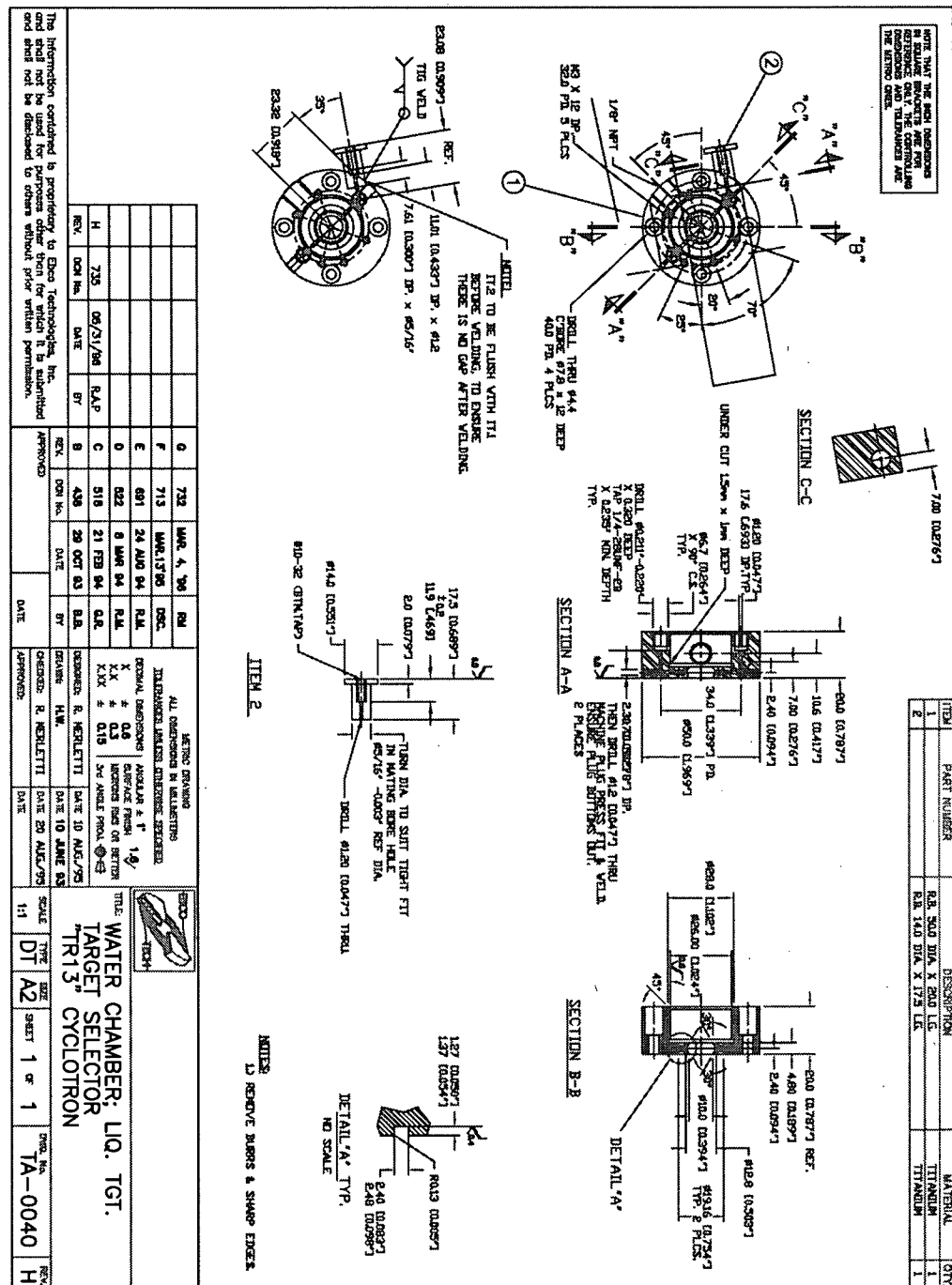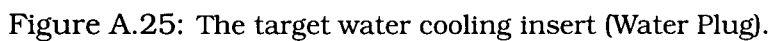
Figure A.22: The target collimator.

Figure A.23: The helium window.

Figure A.24: The target body.

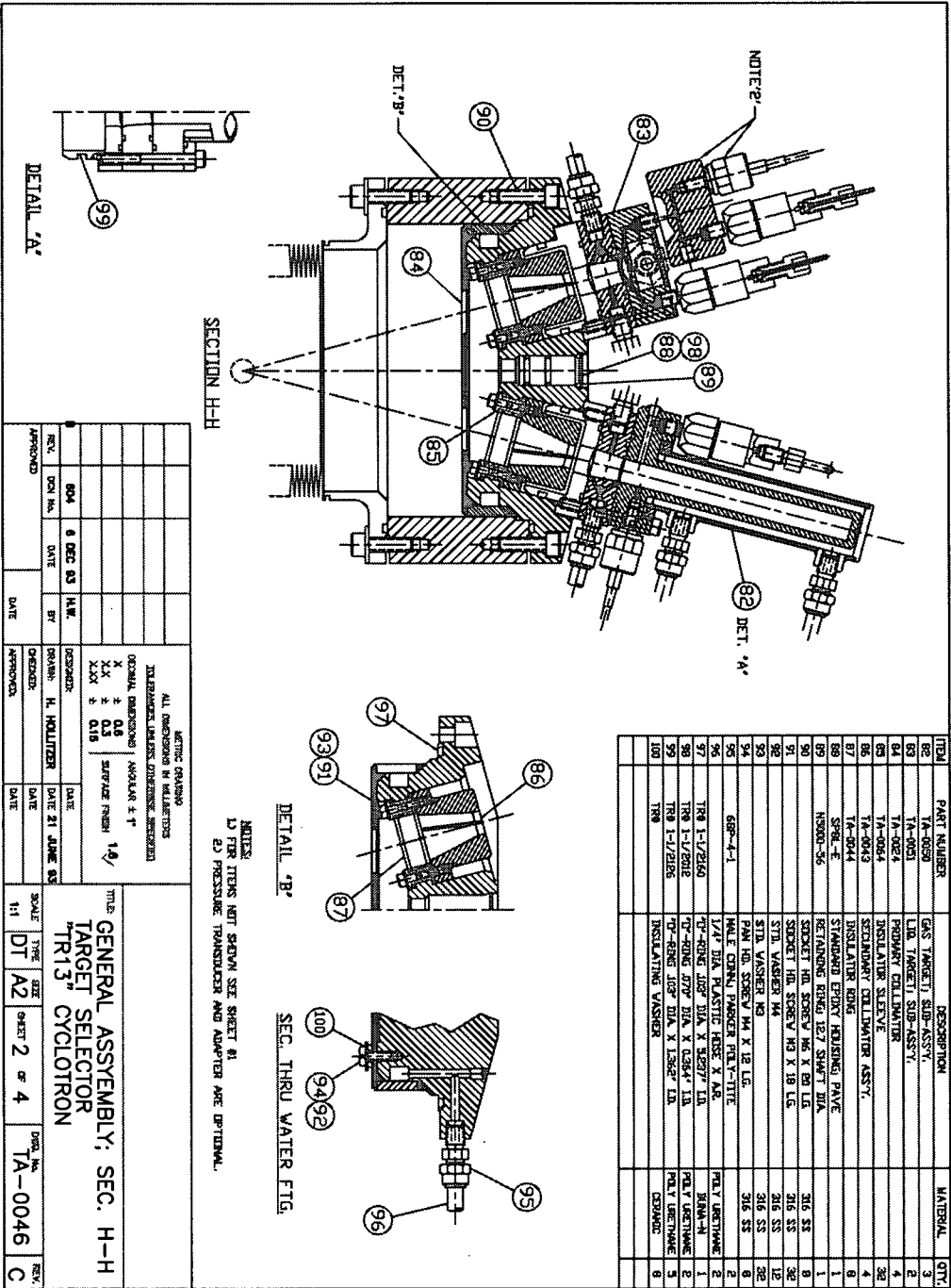Figure A.25: The target water cooling insert (Water Plug).

Figure A.26: The target selector, showing how the targets are mounted.